Draft version February 10, 2022
Typeset using LaTeX **preprint** style in AASTeX61



# STANDING SAUSAGE PERTURBATIONS IN SOLAR CORONAL LOOPS WITH DIFFUSE BOUNDARIES: AN INITIAL-VALUE-PROBLEM PERSPECTIVE

Bo Li,[1] Shao-Xia Chen,[1] and Ao-Long Li[1]

[1] *Shandong Provincial Key Laboratory of Optical Astronomy and Solar-Terrestrial Environment, Institute of Space Sciences, Shandong University, Weihai 264209, China*

Submitted to ApJ

## ABSTRACT

Working in pressureless magnetohydrodynamics, we examine the consequences of some peculiar dispersive properties of linear fast sausage modes (FSMs) in one-dimensional cylindrical equilibria with a continuous radial density profile ($\rho_0(r)$). As recognized recently on solid mathematical grounds, cutoff axial wavenumbers may be absent for FSMs when $\rho_0(r)$ varies sufficiently slowly outside the nominal cylinder. Trapped modes may therefore exist for arbitrary axial wavenumbers and density contrasts, their axial phase speeds in the long-wavelength regime differing little from the external Alfvén speed. If these trapped modes indeed show up in the solutions to the associated initial value problem (IVP), then FSMs have a much better chance to be observed than expected with classical theory, and can be invoked to account for a considerably broader range of periodicities than practiced. However, with axial fundamentals in active region loops as an example, we show that this long-wavelength expectation is not seen in our finite-difference solutions to the IVP, the reason for which is then explored by superposing the necessary eigenmodes to re-solve the IVP. At least for the parameters we examine, the eigenfunctions of trapped modes are characterized by a spatial extent well exceeding the observationally reasonable range of the spatial extent of initial perturbations, meaning a negligible fraction of energy that a trapped mode can receive. We conclude that the absence of cutoff wavenumbers for FSMs in the examined equilibrium does not guarantee a distinct temporal behavior.

*Keywords:* magnetohydrodynamics (MHD) — Sun: corona — Sun: magnetic fields — waves

Corresponding author: Bo Li
bbl@sdu.edu.cn

## 1. INTRODUCTION

There have been abundant observational instances of low-frequency waves and oscillations in the structured solar corona (see, e.g., the reviews by Banerjee et al. 2007; De Moortel & Nakariakov 2012; Wang 2016; Nakariakov et al. 2016). Combined with magnetohydrodynamic (MHD) wave theory, these observations can help deduce the atmospheric parameters that prove difficult to directly measure, thereby constituting the field of "coronal seismology" (see e.g., the reviews by Nakariakov & Verwichte 2005; Nakariakov & Kolotkov 2020; also the textbook by Roberts 2019). Evidently, a physical interpretation needs to be assigned to an observed oscillatory signal for it to be seismologically exploited. For this purpose, it has been customary to contrast observations with the theoretical expectations for waves in field-aligned cylinders that are structured only in the radial direction and in a step form (developed by e.g., Wentzel 1979; Spruit 1982; Edwin & Roberts 1983, hereafter ER83; also Zajtsev & Stepanov 1975; Cally 1986). It turns out that this apparently simple equilibrium supports a rich variety of waves, and we restrict ourselves to the fast family (see Wang et al. 2021, for the most recent review on the slow family). Indeed, radial fundamental kink modes in the sense of Goossens et al. (2009, 2012) have been amply identified and put to seismological practice (see the review by Nakariakov et al. 2021). As an outcome, the spatial variations of the magnetic field strength were deduced not only for individual active regions (ARs, Anfinogentov & Nakariakov 2019) but also over a substantial fraction of the lower corona (Yang et al. 2020).

Candidate fast sausage modes (FSMs), however, have only been sporadically reported in coronal observations (see Li et al. 2020, for the most recent review). As detailed therein, this rarity is intimately connected to the cutoff axial wavenumbers $k_{\rm cutoff}$, to explain which it suffices to consider the pressureless MHD. In fact, we will adopt pressureless MHD throughout, and additionally restrict ourselves to flare loops and AR loops as wave-guiding inhomogeneities [1]. Let $R$ denote the cylinder radius, and $\rho_{\rm i}$ ($\rho_{\rm e}$) the internal (external) density with $\rho_{\rm i} > \rho_{\rm e}$. Likewise, let $v_{\rm Ai}$ ($v_{\rm Ae}$) represent the internal (external) Alfvén speed. Standard analysis of the eigenvalue problem (EVP) on a laterally open domain then yields that FSMs in an ER83 equilibrium possess a series of $k_{{\rm cutoff},m} = j_{0,m}/(R\sqrt{\rho_{\rm i}/\rho_{\rm e}-1})$, where $j_{0,m}$ is the $m$-th zero of Bessel $J_0$ with $m = 1, 2, \cdots$ (e.g., Roberts et al. 1984; Vasheghani Farahani et al. 2014). Now consider an open system unbounded in both the axial ($z$) and radial ($r$) directions, and suppose that a cylinder is perturbed by an axisymmetric perturbation localized both radially and axially. The pertinent two-dimensional initial value problem (2D IVP) has been examined rather extensively, with the majority of solutions found by directly evolving the MHD equations (e.g., Shestov et al. 2015; Yu et al. 2016a, 2017). Physical insights, on the other hand, can also be gleaned from a modal approach, which was discussed heuristically by Edwin & Roberts (1986) and made more formal by Berghmans et al. (1996). Our study makes frequent reference to Oliver et al. (2015, hereafter ORT15), who were the first to offer an explicit expression for the solution to the 2D IVP. Noting that a continuous range of axial wavenumbers ($k$) is involved, Equation (25) in ORT15 expresses the solution as the summation of the contributions associated with an individual $k$, which in turn were written as the superposition of eigenmodes with individual angular frequencies ($\omega$, hereafter "frequency" for brevity). A finite number of discrete $\omega$ pertaining to proper eigenmodes

[1] Sausage perturbations in flare current sheets have also been invoked to account for, say, some fine structures in decimetric type IV radio bursts (Karlický et al. 2011; Jelínek & Karlický 2012; also Li et al. 2020 and references therein). We refrain from discussing such observations to avoid the intricacies that cannot be addressed with pressureless MHD. In fact, we decide to leave out sausage modes in slab-type configurations altogether for the ease of description, even though they have been extensively examined (e.g., Murawski & Roberts 1993; Nakariakov et al. 2004; Pascoe et al. 2013; Yu et al. 2016b; Kolotkov et al. 2021). The approach we are to use, however, is sufficiently general.

(or "trapped modes" in physical terms) are relevant only when $k > k_{\rm cutoff,1}$, whereby the periodicity is consistently $\lesssim 2\pi/(k_{\rm cutoff,1}v_{\rm Ae}) \approx 2.6\sqrt{1-\rho_{\rm e}/\rho_{\rm i}}(R/v_{\rm Ai}) < 2.6R/v_{\rm Ai}$. Regardless of $k$, however, a continuum of improper eigenmodes is always involved, the associated $\omega$ extending from $kv_{\rm Ae}$ out to infinity. The point is, only proper modes survive in the sausage wavetrains sampled sufficiently far from the exciter, the characteristic periodicities therefore being similar to the transverse Alfvén time $R/v_{\rm Ai}$. If an individual $k$ is examined as happens for standing modes, then one finds by directly evolving the MHD equations that $R/v_{\rm Ai}$ consistently characterizes FSMs regardless of $k$ (e.g., Terradas et al. 2007; Nakariakov et al. 2012; Guo et al. 2016; Lim et al. 2020). While this result is much expected for $k > k_{\rm cutoff,1}$, its physical understanding for the opposite situation is a bit involved given the likely contributions due to improper modes with $\omega$ not far exceeding $kv_{\rm Ae}$ (ORT15, see also our Appendix A). The quick answer is that, the interference of the improper modes tends to make their superposition favor a discrete set of periods $P_{\rm leaky}$ that pertain to the so-called "leaky modes" (Andries & Goossens 2007, and references therein), and $P_{\rm leaky}$ is well known to be either similar to or substantially shorter than $2\pi/(k_{\rm cutoff,1}v_{\rm Ae})$ (e.g., Meerson et al. 1978; Cally 1986; Kopylova et al. 2007). The damping time of the discrete leaky modes ($\tau_{\rm leaky}$) is also known to offer a shortcut estimate for the timescale characterizing the wave attenuation, the result being that $\tau_{\rm leaky}/P_{\rm leaky} \approx (\rho_{\rm i}/\rho_{\rm e})/\pi^2$ (e.g., Kopylova et al. 2007). Two primary reasons are now clear to account for the rarity of candidate coronal FSMs. First, $R/v_{\rm Ai}$ typically evaluates to at most a couple of tens of seconds, thereby demanding a high instrumental cadence and ruling out the possibility for typical (extreme) ultraviolet instruments to resolve an FSM (see Su et al. 2012; Tian et al. 2016, for exceptions). Second, there tends to be a stringent requirement on instrumental sensitivity as well. For AR loops, that they are thin and tenuous means that FSMs tend to be detectable only as wavetrains, which are indeed compatible with a number of high-cadence ground-based measurements in visible light during total eclipses (e.g., Williams et al. 2002; Katsiyannis et al. 2003; Samanta et al. 2016). For flare loops, that they are thick and dense means that FSMs have a better chance to be detected both as wavetrains and standing modes, provided once again that the instrumental cadence is sufficient (see Li et al. 2020, and references therein). This explains why candidate coronal FSMs reported so far have been primarily connected to radio measurements of short-period quasi-periodic pulsations (QPPs, see the recent reviews by McLaughlin et al. 2018; Zimovets et al. 2021).

With the ER83 equilibrium apparently idealized, one may argue that cutoff wavenumbers are not inherent to coronal FSMs in reality. Indeed, there have been a considerable number of theoretical studies that extend ER83 by incorporating various aspects of reality (see Li et al. 2020, and references therein). Among these, we focus on the equilibria that differ from ER83 only by replacing the step density profile with a continuous one, the reason being that a generic guiding principle can be established to tell when cutoff wavenumbers exist (Lopin & Nagorny 2015a, hereafter LN15; also Lopin & Nagorny 2015b). Let $R$ now refer to some mean cylinder radius, and let the subscript i (e) refer to the equilibrium quantities at the cylinder axis (infinitely far from the cylinder). The radial profile for the equilibrium density $\rho_0(r)$ can then be described in a generic form $\rho_0(r) = \rho_{\rm e} + (\rho_{\rm i} - \rho_{\rm e})f(r)$, where the function $f(r)$ evaluates to unity (zero) when $r = 0$ ($r \to \infty$). Restrict ourselves to the case where $f(r)$ is monotonical. With Kneser's oscillation theorem, LN15 were the first to point out that cutoff wavenumbers exist only when $r^2 f(r)$ does not diverge when $r$ approaches infinity. This expectation was then verified numerically by Li et al. (2018), one example being for the so-named "outer $\mu$" profile where $f(r)$ is identically unity for $r < R$ but of the form $(r/R)^{-\mu}$ otherwise.

Figure 8 therein indicates that for the $m$-th radial harmonic ($m = 1, 2, \cdots$), no cutoff wavenumber exists (or equivalently $k_{\mathrm{cutoff},m} = 0$) when $\mu < 2$, whereas the combination $(k_{\mathrm{cutoff},m}R)\sqrt{\rho_{\mathrm{i}}/\rho_{\mathrm{e}} - 1}$ increases monotonically from unity for $\mu = 2$ to $j_{0,m}$ for a step profile ($\mu = \infty$).

Some important consequences arise for FSMs when cutoff wavenumbers are absent. Theoretically, the dispersive properties of FSMs in this situation are distinct from FSMs in ER83 in two aspects, one being that trapped modes are allowed regardless of the axial wavenumber $k$ or the density contrast $\rho_{\mathrm{i}}/\rho_{\mathrm{e}}$, and the other being that FSMs tend to be weakly dispersive for small $k$ with axial phase speeds only marginally smaller than $v_{\mathrm{Ae}}$ (e.g., Figure 3 in LN15, and Figure 7 in Yu et al. 2017). With the former distinction evident, we note that trapped FSMs in ER83 are highly dispersive at least when $k$ is not far larger than a cutoff (e.g., Edwin & Roberts 1983; Roberts et al. 1983). Observationally, these two distinctions offer a richer possibility for interpreting oscillatory signals, to illustrate which we consider a spatially resolved QPP measured with the Nobeyama RadioHeliograph (NoRH) as reported by Kupriyanova et al. (2013). As detailed therein, multiple periodicities were simultaneously found, with the associated spatial distributions of the spectral power strongly indicating an axial fundamental together with its overtones in the involved flare loop. Contrasting the observations with the canonical ER83 theory, the authors deduced that these standing modes belong to the kink family, and FSMs were ruled out because of their dispersive properties. However, adopting density profiles similar to the "outer $\mu$" one with $\mu < 2$, both LN15 and Lopin & Nagorny (2019) suggested that the observations may be interpreted as FSMs as well. Put to seismology, this interpretation returned values for the internal Alfvén speed $v_{\mathrm{Ai}}$ that may differ considerably from those returned with the interpretation in terms of kink modes, for which purpose we quote $\sim 1100$ km s$^{-1}$ from Lopin & Nagorny (2019, section 6) and $\sim 1750$ km s$^{-1}$ from Kupriyanova et al. (2013, section 5.1). Strictly speaking, a comparison between the two sets of $v_{\mathrm{Ai}}$ is not straightforward because Lopin & Nagorny (2019) adopted pressureless MHD whereas a finite gas pressure is considered in Kupriyanova et al. (2013) [2]. Our point is that the disappearance of cutoff wavenumbers for FSMs as a result of some straightforward departure of the equilibrium from ER83 can offer more physical interpretations for observations in the first place, and enable more seismological possibilities afterwards.

Some further consequence arises if we now focus on standing FSMs in AR loops. For the ease of description, let us recall that we consistently work in pressureless MHD, and adopt the customary assumption that sees AR loops as straight, density-enhanced, field-aligned cylinders. We further assume that the radial density distribution is of the "outer $\mu$" type, which is reasonable but admittedly difficult to prove or disprove (e.g., Aschwanden et al. 2003; Goddard et al. 2017). In addition, we assume that lower coronal eruptions (LCEs), the primary exciter for the much-observed large-amplitude radial fundamental kink modes (Zimovets & Nakariakov 2015; Nechaeva et al. 2019), can deposit a non-negligible amount of energy as axisymmetric perturbations to AR loops as well. Note that this assumption is not that bold but has been implied in the interpretation of rapidly propagating waves as sausage wavetrains (see the review by Roberts 2008, and references therein). For our purposes, it suffices to consider only axial fundamentals. With dimensionless cutoff wavenumbers $k_{\mathrm{cutoff}}R \geq 1/\sqrt{\rho_{\mathrm{i}}/\rho_{\mathrm{e}} - 1}$ when $\mu \geq 2$, one finds that $k_{\mathrm{cutoff}}R \geq 1/3$ given the typical range of $[2, 10]$

[2] Given that flare loops tend to be dense and hot, one may question whether it is justifiable to adopt pressureless MHD. However, this issue is unlikely to be restrictive provided that the seismologically deduced $v_{\mathrm{Ai}}$ is understood as the transverse fast speed (see Chen et al. 2016). However, caution needs to be exercised when one assesses how FSMs are influenced by the curvature and lateral expansion of flare loops, both effects being observationally relevant but nonetheless not addressed here (for more discussions, see e.g., Pascoe et al. 2009 and Pascoe & Nakariakov 2016 as well as the references both therein and in Li et al. 2020).

quoted for the density contrast $\rho_{\rm i}/\rho_{\rm e}$ (Aschwanden et al. 2004). One further finds that $kR = \pi R/L \lesssim \pi/15$ in view of the measurements of widths and lengths for AR loops imaged in EUV (Schrijver 2007, Figure 1). Standing FSMs, at least axial fundamentals, are therefore unlikely to be observable for two reasons. One is that their periodicities will be $\sim R/v_{\rm Ai}$ and therefore short, and the other is that they tend to experience rapid attenuation as well. Let us stress that these two signatures have not been explicitly shown for this particular "outer $\mu$" profile but are expected with the studies on 1D IVPs addressing standing FSMs in the leaky regime for an ER83 equilibrium (e.g., Terradas et al. 2007; Nakariakov et al. 2012). Now consider those AR loops with $\mu < 2$. Given the absence of cutoff wavenumbers, the system is expected to settle to a trapped mode or some combination of trapped modes, the quality of the oscillatory signals being therefore sufficiently high. Likewise, the periodicites will be eventually characterized by the longitudinal Alfvén time $L/v_{\rm Ae}$, which can be readily resolved with, say, the majority of available UV/EUV instruments. In fact, both expectations have already been invoked in seismological applications, albeit in the context of flare loops (LN15, Lopin & Nagorny 2019). Supposing that AR loops with $\mu < 2$ are not uncommon, one further deduces that a substantial fraction of kink oscillations will be mixed with standing FSMs when LCEs occur. As advocated by Chen et al. (2015) and Guo et al. (2016), the simultaneous observations of multiple modes of distinct nature will then considerably mitigate the non-uniqueness issue inherent to coronal seismology (see Arregui & Goossens 2019, for dedicated remarks) [3]. However, standing FSMs have not been reported or even implicated in observations of oscillating AR loops to our knowledge. An obvious excuse is that observers have nearly exclusively adopted the ER83 framework and therefore dismissed the possibility that FSMs may possess periodicities $\gtrsim 2L/v_{\rm Ae}$ altogether [4]. Our point, however, is that this possibility is expected solely on the basis of EVP analyses on an open domain, and one has yet to demonstrate that FSMs with periodicities $\gtrsim 2L/v_{\rm Ae}$ do exist as solutions to the pertinent IVP.

Focusing on sausage oscillations in AR loops with the "outer $\mu$" family of density profile, we intend to address the question "Does the absence of cutoff wavenumbers guarantee a temporal behavior that is distinct from the situation where cutoff wavenumbers are present?" We decompose this question into two interconnected aspects. One, how does the value of $\mu$ influence the timescale that characterizes the energy attenuation? Two, does the transverse or longitudinal Alfvén time characterize the periodicity when a wave signal is sufficiently strong? This manuscript is structured as follows. Section 2 formulates the IVP for a radially open system, which is then solved with a direct finite-difference (FD) approach in Section 3. While the answer to our question is already clear in the FD solutions, Section 4 moves on to re-solve the IVP by superposing eigen-solutions to the relevant EVP on a closed domain. These modal solutions are presented for more than just cross-validation purposes. Rather, they help quantify the specific contributions from individual frequencies. By experimenting with various domain sizes, we will better connect the solutions to our IVP with the

[3] Simultaneous observations of multiple modes are rare. Our point is that the more information one gathers from observations, the better the to-deduce quantities can be constrained. Take the much-employed kink oscillations in AR loops. Their seismological applications significantly benefit from such additional information as the different damping characteristics in different stages of their temporal evolution (e.g., Hood et al. 2013; Ruderman & Terradas 2013; Pascoe et al. 2016; Guo et al. 2020). Likewise, additional information can be gleaned from the transverse distributions of the EUV emissions from AR loops (see Pascoe et al. 2018 and also Goddard et al. 2017). On this aspect we note that a to-deduce parameter may still be constrained by such techniques as model averaging within the Bayesian framework even when observations do not favor one particular formulation out of many candidate formulations that involve this parameter (see the review by Arregui 2018, and references therein).

[4] The reason for FSMs to be excluded is more related to the fact that the relevant periodicities were found in the transverse displacements of AR loops. See Appendix C for more on this aspect.

theoretical expectations from the analyses of EVPs on an open domain. Section 5 summarizes this study, ending with some concluding remarks.

## 2. PROBLEM FORMULATION

We adopt pressureless ideal MHD as our theoretical framework, in which the primitive variables are the mass density $\rho$, velocity $\boldsymbol{v}$, and magnetic field $\boldsymbol{B}$. The equilibrium quantities are denoted with a subscript 0, and the equilibrium is taken to be static ($\boldsymbol{v}_0 = 0$). Working in a cylindrical coordinate system $(r, \theta, z)$, we take the equilibrium magnetic field to be uniform and directed in the $z$-direction ($\boldsymbol{B}_0 = B_0 \boldsymbol{e}_z$). Seeing AR loops as density-enhanced cylinders with some mean radius $R$, we assume that the equilibrium density ($\rho_0$) depends only on $r$ and decreases from $\rho_{\rm i}$ at the cylinder axis ($r = 0$) to $\rho_{\rm e}$ infinitely far from the cylinder ($r \to \infty$). The Alfvén speed is defined by $v_{\rm A}^2 = B_0^2/(\mu_0 \rho_0)$ with $\mu_0$ being the magnetic permeability of free space. From here onward, by "internal" (subscript i) and "external" (subscript e) we consistently refer to the equilibrium quantities evaluated at $r = 0$ and $r \to \infty$, respectively. The internal (external) Alfvén speed is therefore denoted by $v_{\rm Ai}$ ($v_{\rm Ae}$).

### 2.1. *Preliminary Formulation of the Initial Value Problem*

We now formulate the preliminary version of the initial value problem (IVP) in a radially open system. Let the subscript 1 denote small-amplitude perturbations to the equilibrium. Specializing to sausage perturbations ($\partial/\partial\theta = 0$), the linearized, pressureless, ideal MHD equations read

$$\rho_0 \frac{\partial v_{1r}}{\partial t} = \frac{B_0}{\mu_0} \left( \frac{\partial B_{1r}}{\partial z} - \frac{\partial B_{1z}}{\partial r} \right), \tag{1}$$

$$\frac{\partial B_{1r}}{\partial t} = B_0 \frac{\partial v_{1r}}{\partial z}, \tag{2}$$

$$\frac{\partial B_{1z}}{\partial t} = -B_0 \frac{1}{r} \frac{\partial}{\partial r} \left( r v_{1r} \right) \ . \tag{3}$$

With coronal cylinders bounded by the planes $z = 0$ and $z = L$ in mind, the following ansatz

$$\begin{aligned} v_{1r}(r, z; t) &= \hat{v}(r; t) \sin(kz), \\ B_{1r}(r, z; t) &= \hat{B}_r(r; t) \cos(kz), \\ B_{1z}(r, z; t) &= \hat{B}_z(r; t) \sin(kz), \end{aligned} \tag{4}$$

is appropriate for axial standing modes, with $k = n\pi/L$ being the quantized axial wavenumber ($n = 1, 2, \cdots$). Equations (1) to (3) then become

$$\rho_0 \frac{\partial \hat{v}}{\partial t} = -\frac{B_0}{\mu_0} \left( k \hat{B}_r + \frac{\partial \hat{B}_z}{\partial r} \right), \tag{5}$$

$$\frac{\partial \hat{B}_r}{\partial t} = k B_0 \hat{v}, \tag{6}$$

$$\frac{\partial \hat{B}_z}{\partial t} = -B_0 \frac{1}{r} \frac{\partial}{\partial r} \left( r \hat{v} \right) \ . \tag{7}$$

Without loss of generality, the initial conditions (ICs) are specified as

$$\hat{v}(r, t = 0) = u(r), \tag{8}$$

$$\hat{B}_r(r, t = 0) = \hat{B}_z(r, t = 0) = 0. \tag{9}$$

The boundary condition (BC) at the cylinder axis ($r = 0$) reads

$$\hat{v} = \hat{B}_r = \partial \hat{B}_z / \partial r = 0, \tag{10}$$

whereas the BC at $r \to \infty$ is irrelevant.

It proves necessary to examine the energetics associated with the IVP as well. Let $V$ refer to a volume $V$ bounded laterally by a cylindrical surface with radius $r$ and horizontally by the planes $z = 0$ and $z = L$. One then finds from Equations (5) to (7) that

$$E_{\rm tot}(r,t) - E_{\rm tot}(r,t=0) = -F(r,t), \tag{11}$$

where

$$E_{\rm tot}(r,t) = \pi L \int_0^r (r'dr') \left\{ \frac{1}{2}\rho_0(r')\hat{v}^2(r',t) + \frac{1}{2\mu_0}\left[\hat{B}_r^2(r',t) + \hat{B}_z^2(r',t)\right] \right\} , \tag{12}$$

$$F(r,t) = \pi L \int_0^t dt' \left[ r\hat{p}_{\rm tot}(r,t')\hat{v}(r,t') \right] . \tag{13}$$

Here a common factor $\pi L$ is retained to ensure that $E_{\rm tot}(r,t)$ represents the instantaneous total energy in $V$, while $F(r,t)$ represents the cumulative energy loss from $V$. Furthermore, $\hat{p}_{\rm tot} = B_0 \hat{B}_z/\mu_0$ is connected to the Eulerian perturbation of total pressure. Evidently, the terms in the square parentheses in Equation (13) stem from the radial component of the Poynting vector.

### 2.2. *Reformulation of the IVP and Parameter Specification*

For mathematical convenience, Equations (5) to (10) are reformulated to the following form.

**IVP 1** *Solutions are sought for the following equation*

$$\frac{\partial^2 \hat{v}}{\partial t^2} = v_{\rm A}^2(r) \left( \frac{\partial^2 \hat{v}}{\partial r^2} + \frac{1}{r}\frac{\partial \hat{v}}{\partial r} - \frac{\hat{v}}{r^2} - k^2 \hat{v} \right), \tag{14}$$

*subjected to the ICs*

$$\hat{v}(r, t=0) = u(r), \quad \frac{\partial \hat{v}}{\partial t}(r, t=0) = 0, \tag{15}$$

*togeter with the BC*

$$\hat{v}(r=0, t) = 0, \tag{16}$$

*on a domain spanning from $r = 0$ to $\infty$.*

Necessary for energetics considerations, $\hat{B}_r(r,t)$ and $\hat{B}_z(r,t)$ can be found with $\hat{v}(r,t)$ by integrating Equations (6) and (7) from the initial state (9).

We proceed to make IVP 1 more specific. The equilibrium density distribution is chosen to be the "outer $\mu$" profile in Yu et al. (2017), namely

$$\begin{aligned} \rho_0(r) &= \rho_{\rm e} + (\rho_{\rm i} - \rho_{\rm e}) f(r), \\ f(r) &= \begin{cases} 1, & 0 \le r \le R, \\ (r/R)^{-\mu}, & r \ge R. \end{cases} \end{aligned} \tag{17}$$

Here $\mu \geq 1$ measures the steepness of $\rho_0(r)$ outside the cylinder. We focus on axial fundamentals ($k = \pi/L$). In addition, we specify the initial perturbation in Equation (15) as

$$\frac{u(r)}{v_{\rm Ai}} = \begin{cases} \sin^3(\pi r/\Lambda), & 0 \leq r \leq \Lambda, \\ 0, & r \geq \Lambda, \end{cases} \tag{18}$$

which is localized within $r = \Lambda$ and prescribed to be sufficiently smooth with a magnitude arbitrarily set to be the internal Alfvén speed ($v_{\rm Ai}$).

The solution to IVP 1 is fully determined by the dimensionless paramters $[\rho_{\rm i}/\rho_{\rm e}, \mu; L/R; \Lambda/R]$, among which we see $\mu$ as the primary adjustable one. The density contrast and loop length-to-radius ratio are fixed at $[\rho_{\rm i}/\rho_{\rm e}, L/R] = [2.25, 15]$, both close to the lower end of but nonetheless within the accepted range for AR loops (e.g., Aschwanden et al. 2004; Schrijver 2007). We take $\Lambda = 4\ R$ unless otherwise specified. Figure 1a illustrates our equilibrium, and the blue arrows represent the initial velocity field in any cut through the cylinder axis as appropriate for an axial fundamental. Specializing to IVP 1, Figure 1b shows the radial profiles for $u(r) = \hat{v}(r, t = 0)$ (the blue dashed curve) and for the equilibrium density ($\rho_0$, the solid curves). Two values are adopted for $\mu$, one being 1.5 (the black curve) and the other being 5 (red). As already stressed, FSMs do not suffer from cutoff wavenumbers $k_{\rm cutoff}$ for $\mu < 2$. When $\mu \geq 2$, $k_{\rm cutoff} R$ always exceeds $1/\sqrt{\rho_{\rm i}/\rho_{\rm e} - 1}$ and therefore $\gtrsim 0.89$ with the chosen $\rho_{\rm i}/\rho_{\rm e}$, making trapped modes irrelevant for the chosen $kR = \pi/15 \approx 0.21$.

## 3. FINITE-DIFFERENCE SOLUTIONS

We choose to solve IVP 1 with two independent methods, one being a finite-difference (FD) approach, and the other being a modal approach involving eigenmodes for the EVPs on either a closed or an open domain. In practice, the FD approach turns out to be orders-of-magnitude less time-consuming, and is therefore more suitable for parametric studies.

### 3.1. *Method*

The development of our FD code starts with constructing a system of code units, the details of which are irrelevant because we will consistently present our results as dimensional quantities. Equation (14) is discretized on a uniform grid with spacing $\Delta r = 0.01\ R$ over a domain of $[0, r_{\rm M}]$. All spatial derivatives are approximated by centered differences, yielding second-order accuracy in space. The time-marching is handled in a leap-frog manner with a uniform timestep $\Delta t$. A ghost timestep at $t = -\Delta t$ is introduced to account for the IC for $\partial\hat{v}/\partial t$, ensuring that the scheme is second-order accurate in time as well. The timestep is specified as $\Delta t = c\Delta r/v_{\rm Ae}$, where the Courant number $c$ is chosen to be $\sim 0.4$ to ensure numerical stability. Grid convergence tests are conducted to ensure that varying the grid spacing or the Courant number does not influence our results. More importantly, we make sure that the location of the outer boundary $r_{\rm M}$ does not affect our FD solutions either.

### 3.2. *Numerical Results*

Figure 2 presents our FD solutions by showing the distribution of the radial speed $\hat{v}$ in the $r-t$ plane. We contrast two cases with the steepness parameter being (a) $\mu = 1.5$ and (b) $\mu = 5$, respectively. One sees from Figure 2 that the temporal evolution in both cases is characterized by some dispersive propagation of the axisymmetric disturbance. To proceed, we note that the disturbances belong to the fast family, and the local fast speed is equivalent to the local Alfvén speed in pressureless

MHD. For the ease of description, the most prominent wavefronts are singled out and labeled such that the + (−) sign pertains to outward (inward) propagation. When necessary, the same label will be used to denote the associated wake as well. The following features can then be readily told in both cases, to describe which it suffices to consider only Figure 2a. Firstly, the initial perturbation splits into two wavefronts manifested as the two bright stripes labeled $1_+$ and $1_-$. While not that evident, wavefront $1_-$ is actually accompanied by a wake appearing as a narrow dark stripe. At least a substantial fraction of both wavefront $1_-$ and its wake then make it into the cylinder ($r < R$), as evidenced by the change of slope of the stripe. Here by "a substantial fraction" we mean that some reflection is expected but difficult to identify. Secondly, once reaching the cylinder axis ($r = 0$), wavefront $1_-$ is reflected to form wavefront $2_+$ which then propagates outward as a dark stripe. The change from a bright to a dark stripe for essentially the same wavefront is simply because $\hat{v}$ necessarily reverses sign at the cylinder axis, which acts as a rigid wall in the present context (see also Berghmans et al. 1996, hereafter BDBG96). In this sense, the bright stripe following wavefront $2_+$, namely wake $2_+$, is actually the reflected wake $1_-$. Thirdly, the partial reflection of wake $2_+$ around the cylinder boundary ($r = R$) then leads to wavefront $3_-$, part of which is guided by the dashed curve. Wavefront $4_+$ then result from the reflection of wavefront $3_-$ at the cylinder axis. Having described these common features, we note that some differences nonetheless exist between the two cases. For instance, wavefront $3_-$ is easier to tell for $\mu = 5$ than for $\mu = 1.5$. This is understandable because the case with $\mu = 5$ corresponds to a steeper $v_{\rm A}$ profile around the cylinder boundary and hence a stronger partial reflection there.

The slight differences notwithstanding, in both cases one expects a continuous decrease for the wave energy in the cylindrical volume $V$ bounded by $r = \Lambda$, namely where the initial perturbation is applied. This expectation is indeed true [5], to demonstrate which we display the temporal variations of the total energy in $V$ ($E_{\rm tot}$, the dashed curves) and the cumulative energy loss from $V$ ($F$, dash-dotted) in Figure 3. The sum $E_{\rm tot} + F$ is further given by the solid curves. We discriminate between the cases with $\mu = 1.5$ and $\mu = 5$ by different colors. From the solid curves one sees that energy conservation is maintained remarkably well, to quantify which we quote an accuracy of better than 0.05% for all FD computations. Examining the dashed curves, one sees that $E_{\rm tot}$ shows a couple of plateaus with the behavior of $E_{\rm tot}$ for $\mu = 5$ around $t \sim 5\ R/v_{\rm Ai}$ being an example. In view of Equations (11) and (13), these plateaus appear simply because the radial component of the Poynting flux tends to vanish therein. More importantly, $E_{\rm tot}$ rapidly decreases with time, with the two most prominent intervals readily accounted for by the passage of wavefronts $1_+$ and $2_+$ (see Figure 2). Virtually no energy is left in $V$ when $t \gtrsim 7\ R/v_{\rm Ai}$, which is true for $\mu = 5$ and $\mu = 1.5$ alike.

The rapid attenuation of wave energy can be told, in a more straightforward way, by directly showing the temporal evolution of the radial speed itself $\hat{v}$. This is done in Figure 4 where we plot $\hat{v}$ at $r = R$ and use different colors to discriminate different values of $\mu$. We note that the FD solutions are shown by the solid curves, labeled "FD open" to reflect that they are found on an open domain. The asterisks, labeled "modal closed", represent the solutions found by superposing the eigenfunctions for the EVP on a closed domain. The details of the modal solutions are not important for now. What matters is that they agree with the FD ones exactly, thereby suggesting the reliability of both sets of

[5] In addition to $\mu$, the value of $\Lambda$ is also varied in the parametric survey to be presented shortly. When $\Lambda \gtrsim 6\ R$, we can discern some very brief time intervals with widths $\lesssim 0.2R/v_{\rm Ai}$ during which the total energy $E_{\rm tot}$ shows an extremely weak increase. However, these intervals are not important for our purposes because they appear exclusively after $E_{\rm tot}$ has already decreased by a factor of $\gtrsim 50$.

solutions. Consider now only the solid curves. With the aid of Figure 2, one readily identifies the first three extrema with wavefronts $1_-$ and $2_+$ as well as wake $2_+$. One further sees one more extremum (two more extrema) in the black (red) curve, the corresponding wavefronts/wakes also identifiable in Figure 2. When discernible, any extremum in the black curve appears later than its counterpart in the red curve. The explanation for this behavior is actually straightforward because the extrema in $\hat{v}(R,t)$ ultimately derive from wavefront $1_-$. One sees from Figure 1 that the local fast speed $v_{\rm A}(r)$ at any $r > R$ is larger for $\mu = 5$ than for $\mu = 1.5$. It therefore takes more time for wavefront $1_-$ to enter the cylinder ($r \leq R$) in the case with $\mu = 1.5$, thereby making the relevant extrema in $\hat{v}(R,t)$ appear later. With this understanding, the spacing between two consecutive prominent extrema, or equivalently the periodicity when the signal is strong, is intimately connected to the passage of the relevant wavefronts/wakes before they appear in $\hat{v}(R,t)$. The end result is that, the periodicity is expected to depend on the details of both the equilibrium density profile and the initial perturbation. In our setup, this translates into the dependence on $\mu$ and $\Lambda$.

Figure 5 quantifies the dependence of the wave behavior on the steepness parameter ($\mu$) for a number of values of the spatial extent of the initial perturbation ($\Lambda$) as labeled. Two quantities are examined, one being the time that it takes for $E_{\rm tot}(\Lambda,t)$ to drop from the initial value by a factor of $\mathrm{e}^4 \approx 55$ ($\tau_{\rm ener}$, Figure 5a) and the other being the temporal spacing between the first two extrema in the $\hat{v}(R,t)$ profile ($\Delta_1$, Figure 5b). Let us examine Figure 5a first, and start by noting that we deliberately choose a rather large factor ($\mathrm{e}^4$) to determine $\tau_{\rm ener}$. We note further that the initial perturbation peaks at $r = \Lambda/2$ (see Equation (18)). Now two prominent features are evident. Firstly, $\tau_{\rm ener}$ at any given $\mu$ increases with $\Lambda$. Secondly, the $\mu$-dependence of $\tau_{\rm ener}$ tends to be weak when $\Lambda \lesssim 2\ R$. Let $V$ still denote the cylindrical volume laterally bounded by $r = \Lambda$. It turns out that the departure of wavefronts $1_+$ and $2_+$ from $V$ is the primary reason for $E_{\rm tot}(\Lambda,t)$ to decrease to the designated threshold (see Figure 2). In particular, $\tau_{\rm ener}$ tends not to be much longer than the time $t_{2+}$ at which wavefront $2_+$ arrives at $r = \Lambda$. In turn, this transit time $t_{2+}$ comprises two components,

$$t_{2+} = t_{1-}(\Lambda/2 \to 0) + t_{2+}(0 \to \Lambda), \tag{19}$$

where the symbols on the right-hand side (RHS) are such that $t_{1-}(\Lambda/2 \to 0)$ represents the time that wavefront $1_-$ spends when traveling from $r = \Lambda/2$ to $r = 0$. For a given $\mu$, both terms on the RHS increase with $\Lambda$, meaning that $t_{2+}$ and hence $\tau_{\rm ener}$ increase monotonically with $\Lambda$. Now move on to the $\mu$-dependence for a given $\Lambda$. When $\Lambda \lesssim 2\ R$, the cylinder exterior ($r > R$) is relevant for determining $t_{2+}$ only by being partially involved in $t_{2+}(0 \to \Lambda)$. When $\Lambda > 2\ R$, however, it is involved in both terms on the RHS of Equation (19). The end result is that, $t_{2+}$ and hence $\tau_{\rm ener}$ are insensitive to $\mu$ when $\Lambda \lesssim 2\ R$ but tend to decrease with $\mu$ when the opposite is true, which is understandable given that the local fast speed $v_{\rm A}(r)$ at any $r > R$ increases with $\mu$.

Now move on to Figure 5b. One sees that $\Delta_1$ possesses a considerably more complicated behavior, by which we mean the features difficult to understand with the simple kinematic considerations that were applied to Figure 5a. Take the cases where $\Lambda = 4\ R$ and $\Lambda = 8\ R$. In both cases, the first and second extrema in the $\hat{v}(R,t)$ profile correspond to wavefronts $1_-$ and $2_+$, respectively. In kinematic terms, the temporal spacing between the two then comprises $t_{1-}(R \to 0)$ and $t_{2+}(0 \to R)$, neither of which is supposed to involve $\Lambda$ or $\mu$. Consequently, the blue and maroon curves are expected to overlap, an expectation evidently at variance with the numerical results. One therefore deduces that $\Delta_1$ embeds some subtleties that the kinematic arguments cannot address, which will become

evident in the modal solutions to be presented shortly. The quick answer is the common sense that $\mu$ is relevant for determining the eigenstructures, while $\Lambda$ determines how the energy in the initial perturbation is distributed among the eigenmodes (see Equation (23)). Important for now is that Figure 5 has already answered the questions we laid out in the Introduction. Firstly, Figure 5a indicates that the energy imparted by the initial perturbation is attenuated within a characteristic timescale $\tau_{\rm ener} \sim \mathcal{O}(\Lambda/v_{\rm Ai})$. If $\Lambda$ is not far different from $R$, then axisymmetric perturbations will rapidly become too weak to detect. Secondly, even if some instrument happens to capture a perturbation immediately after its excitation, Figure 5b indicates that $\Delta_1$ is consistently $\sim \mathcal{O}(R/v_{\rm Ai})$, thereby placing rather stringent demands on the instrumental cadence. Thirdly, for any examined $\Lambda$, no abrupt change is seen in the behavior of $\tau_{\rm ener}$ or $\Delta_1$ when $\mu$ crosses the nominally critical value of two. Put another way, trapped modes are not discernible even though they suddenly appear when $\mu$ drops below two in EVPs on an open domain. We address why in what follows.

## 4. MODAL SOLUTIONS

### 4.1. *Method*

Our modal approach starts with specifying the following EVP on a closed domain.

**EVP 1** *Nontrivial solutions are sought for the following equation*

$$-\omega^2\breve{v} = v_{\rm A}^2(r)\left(\frac{d^2}{dr^2}\breve{v} + \frac{d}{rdr}\breve{v} - \frac{\breve{v}}{r^2} - k^2\breve{v}\right), \tag{20}$$

*defined on a domain of* $[0, d]$ *and subjected to the BCs*

$$\breve{v}(r=0) = \breve{v}(r=d) = 0. \tag{21}$$

Equation (20) is found by replacing $\hat{v}$ with $\mathrm{Re}[\breve{v}(r)\exp(-i\omega t)]$ in Equation (14).

EVP 1 is known to possess the following Sturm-Liouville properties (see BDBG96 for details, even though a step profile is examined therein). First of all, the eigenvalues ($\omega^2$) are positive and form an infinite, discrete, monotonically increasing sequence $\{\omega_l\}$ with respect to the mode number $l = 1, 2, \cdots$. The associated eigenfunction $\breve{v}_l(r)$ can be made and will be seen as real-valued. It then follows that $\breve{v}_l(r)$ possesses $l-1$ nodes inside the domain. In addition, the set $\{\breve{v}_l(r)\}$ is complete and satisfies the orthogonality condition

$$\int_0^d \breve{v}_l(r)\breve{v}_m(r)\rho_0(r)rdr = 0, \tag{22}$$

provided $l \neq m$. Eventually, the solution to IVP 1 can be written as

$$\begin{aligned} \hat{v}^{(d)}(r,t) &= \sum_{l=1}^{\infty} c_l\breve{v}_l(r)\cos(\omega_l t), \\ 0 \leq r \leq d, \quad t &\leq \int_\Lambda^d \frac{dr}{v_{\rm A}(r)}, \end{aligned} \tag{23}$$

where the coefficient $c_l$ measures the contribution from the $l$-th mode,

$$c_l = \frac{\displaystyle\int_0^d u(r)\breve{v}_l(r)\rho_0(r)rdr}{\displaystyle\int_0^d \breve{v}_l^2(r)\rho_0(r)rdr}. \tag{24}$$

The superscript $(d)$ in Equation (23) is meant to indicate that the modal structure depends on the domain size $d$. Here and hereafter, by "modal structure" we further mean the $l$-dependence of $\omega_l$. Expressed formally, $\omega_l$ can be written as

$$\frac{\omega_l R}{v_{\rm Ai}} = \mathcal{F}_l(\rho_{\rm i}/\rho_{\rm e}, \mu; kR; d/R). \tag{25}$$

However, we stress that the modal solution $\hat{v}^{(d)}(r,t)$ itself does not depend on $d$ in the timeframe of validity explicitly given in Equation (23). Physically, this timeframe of validity represents simply the interval when the outermost edge of the perturbation is within the domain of EVP 1.

We now describe some details involved in the evaluation of Equation (23). To start, $[\rho_{\rm i}/\rho_{\rm e}, kR, \Lambda/R]$ is fixed at $[2.25, \pi/15, 4]$ for all modal solutions. In the main text, we contrast only two steepness parameters ($\mu = 1.5$ and $\mu = 5$) but experiment with a substantial number of dimensionless domain sizes ($d/R$). The step profile ($\mu = \infty$) is also of interest, the discussions nonetheless collected in Appendix A. Regardless, we consistently formulate and solve EVP 1 with the general-purpose finite-element code PDE2D (Sewell 1988), which was first introduced into the solar context by Terradas et al. (2006). A uniform grid is adopted if $d/R \leq 150$, otherwise we employ a grid whereby the spacing is uniform for $r \leq 5\ R$ but increases by a constant factor afterwards. We make sure that different grid setups yield consistent solutions to EVP 1. Likewise, we make sure that the number of modes ($l_{\rm max}$) incorporated in the summation in Equation (23) is sufficiently large, meaning that increasing $l_{\rm max}$ does not influence the modal solutions to be analyzed.

Some insights into EVP 1 are further necessary to address the roles of $\mu$ and $d/R$. These are made transparent when Equation (20) is transformed into a Schrödinger form with standard techniques employed by, e.g., BDBG96 and LN15, the result being

$$\begin{aligned} &\frac{d^2\Phi}{dr^2} + Q(r)\Phi = 0, \\ &Q(r) = \frac{\omega^2 - V(r)}{v_{\rm A}^2(r)}. \end{aligned} \tag{26}$$

Here $\Phi(r) = r^{1/2}\breve{v}(r)$ defines some "wave function", while

$$V(r) = v_{\rm A}^2(r)\left(k^2 + \frac{3}{4r^2}\right) \tag{27}$$

defines the potential. Three properties then ensue. One, $\omega_l$ is bound to exceed $kv_{\rm Ai}$ regardless of $\mu$ or $d/R$ (see Appendix B). Two, high-frequency modes with $\omega_l \gg kv_{\rm Ae}$ are permitted regardless of $\mu$ or $d/R$, and they follow the relation $\omega_l \approx l\pi v_{\rm Ae}/d$ when $d/R$ is sufficiently large (also see Appendix B). Three, the spatial behavior of mode functions $\breve{v}(r)$ is determined by the sign of $Q(r)$. We therefore classify the modes into two categories, labeling those with $Q(d) > 0$ ($Q(d) < 0$) as "oscillatory" ("evanescent"). For the ease of description, we see this classification scheme as applicable only to closed systems, but adopt the viewpoint that such terms as "trapped" versus "leaky" (e.g., ER83; Cally 1986) or "proper" versus "improper" (ORT15; also Oliver et al. 2014) apply to open systems. Evidently, an evanescent mode becomes a trapped mode when $d$ goes infinite. Its frequency $\omega_l$ is therefore $d/R$-independent for sufficiently large $d/R$, and is bound to be lower than the "critical frequency" $\omega_{\rm crit} = kv_{\rm Ae}$ because $V(r) \to k^2 v_{\rm Ae}^2$ when $r \to \infty$. Now specialize to our chosen set $[\rho_{\rm i}/\rho_{\rm e}, kR] = [2.25, \pi/15]$. Evanescent modes are possible only when $\mu < 2$. All modes are oscillatory for $\mu \geq 2$, the frequency $\omega_l$ for any $l$ always higher than $\omega_{\rm crit}$ and $d/R$-dependent.

### 4.2. *Numerical Results*

#### 4.2.1. *Frequency Distribution of Modal Contributions*

We fix the domain size to be $d = 50\ R$ in this subsection. As shown by Figure 4, the modal solutions thus constructed agree with their FD counterparts. The dependencies on the mode frequency ($\omega_l$) of the contributions of individual modes are then shown in Figure 6, where the modes are represented by the asterisks and different colors are adopted to discriminate between the two steepness parameters. The critical frequency $\omega_{\rm crit} = kv_{\rm Ae}$ is plotted by the vertical dash-dotted lines for reference. By examining $|c_l|$, Figure 6a overviews the gross contributions from individual modes, where by "gross" we mean that $c_l$ is position-independent (Equation (24)). For $\mu = 1.5$ (the black symbols) and $\mu = 5$ (red) alike, the $\omega_l$-dependence of $|c_l|$ features a number of peaks whose magnitude weakens with $\omega_l$. The modal contributions at the specific location $r = R$ are plotted in Figure 6b, from which one sees that the spatial dependence of $\breve{v}_l(r)$ makes the contributions from modes with $\omega_l \gtrsim 3.5\ v_{\rm Ai}/R$ less pronounced than expected with Figure 6a. Regardless, the point is that $\hat{v}^{(d)}(R,t)$ is dominated by modes with $\omega_l$ higher than but not far higher than $v_{\rm Ai}/R$, in agreement with the periodicities found in Figure 4. More importantly, the lowest mode frequency $\omega_1$ exceeds $\omega_{\rm crit}$, meaning that all modes are oscillatory. This is true not only for $\mu = 5$ but also for $\mu = 1.5$, despite that trapped modes are bound to appear in the latter case for a truly open system.

#### 4.2.2. *Dependence of Modal Structure on Domain Size*

This subsection examines how the modal structure depends on the dimensionless domain size $d/R$, the reasons for doing which are twofold. Firstly, that trapped modes appear for an open system when $\mu < 2$ was found on solid mathematical grounds by LN15. One naturally argues that $d/R$ in Figure 6 is not large enough for an evanescent mode to appear. However, the modal solution (23) does not depend on $d/R$ within the timeframe explicitly given there. Figure 6 then indicates that the contribution from evanescent modes is negligible even if $d/R$ is larger still. We will quantify how negligible this contribution is. Secondly, to our knowledge, the only study involving EVP 1 was conducted by BDBG96 for a step profile. However, the $d/R$-dependence was not of interest and hence only briefly mentioned in Figure 2 therein. We analytically examine this dependence in some detail for step and continuous profiles in Appendices A and B, respectively. The analytical results in turn help better quantify the modal behavior that we find numerically and present in the main text.

We start by examining the $d/R$-dependence of the modal contributions to $\hat{v}^{(d)}(r,t)$. For this purpose we rewrite the modal solution (23) as

$$\hat{v}^{(d)}(r,t) = \sum_{\omega_l < kv_{\rm Ae}} c_l \breve{v}_l(r) \cos(\omega_l t) + \sum_{\omega_l > kv_{\rm Ae}} S_l \breve{v}_l(r) \cos(\omega_l t) \Delta\omega_l, \tag{28}$$

where the second summation accommodates all oscillatory modes whereas the first collects evanescent ones. The frequency spacing

$$\Delta\omega_l = \omega_{l+1} - \omega_l \tag{29}$$

is relevant only for oscillatory modes in Equation (28) but actually defined for all $l$. We further view the combination $S_l \breve{v}_l(r)$ as some local "spectral density", with $S_l$ defined by

$$S_l = \frac{c_l}{\omega_{l+1} - \omega_l}. \tag{30}$$

Why is the modal solution decomposed in such a simple but cumbersome way? We choose to leave a detailed answer until later, and for now stress only that it does not make sense to compare the frequency-dependencies of $c_l\breve{v}_l$ at a specific location between different values of $d/R$ because of the $d/R$-dependence of $\omega_l$. This is made more specific by Figure 7, where we specialize to $r = R$ and display the $\omega_l$-dependencies of the local spectral densities $S_l\breve{v}_l(R)$ for both $\mu = 1.5$ (the black symbols) and $\mu = 5$ (red). Two domain sizes are examined, with the result for $d/R = 50$ (100) represented by the asterisks (pluses). For both values of $\mu$, one sees that the spectral densities for the two values of $d/R$ outline exactly the same curve, even though the mode frequencies are more closely spaced for $d/R = 100$ than for $d/R = 50$. One further sees that all modes remain oscillatory for $\mu = 1.5$ even when $d/R = 100$. In fact, an evanescent mode appears for this $\mu$ only when $d/R \gtrsim 4000$, a remarkably large value that makes it numerically formidable to compute the necessary set of modes to yield a further $\omega_l$-dependence of $S_l\breve{v}_l(R)$. We rather arbitrarily choose a $d/R = 12800$ and compute only two small subsets for each $\mu$, the first (second) comprising those five modes with $\omega_l$ just exceeding $1.5\ v_{\rm Ai}/R$ ($3\ v_{\rm Ai}/R$). The corresponding spectral densities are plotted by the diamonds. For each $\mu$, one then expects to see ten but actually can discern only two diamonds because the mode frequencies in each subset are too close to tell apart. Regardless, the diamonds lie exactly on the curve outlined by the result for any smaller $d/R$, reinforcing the insignificance of evanescent modes despite that one such mode does exist. To be precise, $c_1\breve{v}_1(R)$ for $\mu = 1.5$ evaluates to $3.51 \times 10^{-11}$ in units of $v_{\rm Ai}$ or rather in units of the magnitude of the initial perturbation.

We focus on how the modal structure varies when the domain size varies. For a sequence of $d/R$ as labeled, Figure 8a shows the frequencies ($\omega_l$) of the first 20 modes as horizontal ticks stacked vertically at a given $d/R$, with the results for $\mu = 1.5$ and $\mu = 5$ differentiated by the black and red colors. Note that in this "level scheme", $\omega_l$ is measured in units of the critical frequency ($\omega_{\rm crit}$), and the horizontal dash-dotted line marks $\omega_l = \omega_{\rm crit}$. Two features then follow. By examining the case with $d/R = 50$ for either value of $\mu$, one sees that the frequency spacing $\Delta\omega_l$ becomes increasingly uniform with increasing $l$. As detailed in Appendices A.2 and B, this feature derives from the fact that for any $\mu$ at a sufficiently large $d/R$, the mode frequency $\omega_l$ for large enough $l$ can be approximated by $l\pi v_{\rm Ae}/d$ (Equation (A17)). Slightly surprising is that this approximation is accurate to better than 5% for both $\mu$ when $l$ merely exceeds 11, despite that $l$ is nominally required to be $\gg (d/R)/\pi \approx 15.9$ for Equation (A17) to hold. While not shown, we find that $\omega_l$ may be approximated by $l\pi v_{\rm Ae}/d$ for $l$ beyond its nominal range of validity at other values of $d/R$ as well. Regardless, by "feature 1" we refer to the $\mu$-independent fact that $\omega_l \propto l v_{\rm Ae}/d$ and hence $\Delta\omega_l \propto v_{\rm Ae}/d$ at large $l$ and large $d/R$. Feature 2, on the other hand, concerns the modes with $\omega_l$ that differs little from $\omega_{\rm crit}$. This turns out to be difficult to examine with Figure 8a, because the mode frequencies become increasingly packed when $d/R$ increases. In fact, $\Delta\omega_l$ eventually becomes so small that we choose to exaggerate the fractional difference $\delta_l = \omega_l/\omega_{\rm crit} - 1$ by a factor of $10^5$ in Figure 8b, where the horizontal dash-dotted line again marks $\omega_l = \omega_{\rm crit}$. Now one sees that $\omega_l$ consistently exceeds $\omega_{\rm crit}$ for $\mu = 5$, meaning that the modes are consistently oscillatory. When $\mu = 1.5$, however, the first mode shows up as an evanescent mode for $d/R = 50 \times 3^5 = 12150$, and so does the second mode at the even larger $d/R$.

Figure 9 further examines the modes with $\omega_l$ close to $\omega_{\rm crit}$ for (a) $\mu = 1.5$ and (b) $\mu = 5$. Here the modulus of $\delta_l = \omega_l/\omega_{\rm crit} - 1$ for a given $l$ is displayed as a function of $d/R$ by the solid (dashed) curves when $\delta_l$ is positive (negative). Among the 50 modes examined, one mode out of five is plotted when $l$ ranges from 10 to 50, whereas all the first five are presented. For reference, the eigenfunctions

$\breve{v}_l$ of the first three modes are given by Figure 10 for $\mu = 1.5$ (the left column) and $\mu = 5$ (right). A number of $d/R$ are examined and can be directly read from the figure. Examine the case with $\mu = 5$ first. Figure 9b indicates that $\delta_l$ is positive for all modes, the oscillatory nature of which is made clearer by the spatial behavior of $\breve{v}_l$ in Figure 10. Furthermore, $\delta_l$ for all $l$ follows a $1/d^2$-dependence shown by the blue dash-dotted curve in Figure 9b. We note that this $1/d^2$-dependence is not empirically found but inspired by the analytical behavior of $\delta_l$ for step density profiles when $\delta_l \ll 1$ (see Equation (A11) for details). That this dependence applies to the case $\mu = 5$ reinforces the notion that the mode behavior is qualitatively similar when $\mu > 2$. Now move on to the more interesting case where $\mu = 1.5$. For any of the first three modes, Figure 9a indicates a transition from an oscillatory to an evanescent mode as evidenced by the change of the sign of $\delta_l$ at some critical $(d/R)_{\mathrm{cri},l}$. When $d/R$ becomes larger still, $\delta_l$ and hence $\omega_l$ become independent of $d/R$. In addition, $(d/R)_{\mathrm{cri},l}$ is seen to increase with $l$, a feature that can be readily understood with the left column of Figure 10. Let $D_l$ denote the spatial extent of the eigenfunction of an evanescent mode, meaning mathematically that $Q(r)$ becomes negative when $r > D_l$ (see Equations (26) and (27)). When multiple evanescent modes exist on a sufficiently large domain, their frequencies are necessarily such that $\omega_1 < \omega_2 < \cdots$ because the entire set $\{\omega_l\}$ is a monotonically increasing sequence with respect to $l$. On the other hand, it can readily shown that the potential $V(r)$ eventually approaches $k^2 v_{\mathrm{Ae}}^2$ from below (above) when $\mu < 2$ ($\mu > 2$). It then follows that $D_1 < D_2 < \cdots$. Consequently, $(d/R)_{\mathrm{cri},1}$ is necessarily smaller than $(d/R)_{\mathrm{cri},2}$ for the domain to accommodate the diminishing portion of the eigenfunction of the second mode. In fact, the sequence $(d/R)_{\mathrm{cri},l}$ necessarily increases monotonically with respect to $l$. Figure 9a further indicates that at sufficiently large $d/R$, the oscillatory modes for $\mu = 1.5$ remain characterized by $\delta_l \propto 1/d^2$ unless $\delta_l$ is extremely small.

With the aid of Equation (28), we now offer some general remarks on the dependencies on the steepness parameter $\mu$ of both the modal behavior on a closed domain with large $d/R$ and the solution to IVP 1. However, we choose to focus on the chosen $[\rho_{\mathrm{i}}/\rho_{\mathrm{e}}, kR, \Lambda/R] = [2.25, \pi/15, 4]$ to avoid this manuscript becoming even longer. When $\mu < 2$, more and more evanescent modes appear when $d/R$ increases. With the exception of the first several, the oscillatory modes are such that their frequency spacing $\Delta\omega_l$ starts with a $1/d^2$-dependence before eventually settling to a $1/d$-dependence. All modes are oscillatory when $\mu > 2$, and the corresponding $\Delta\omega_l$ simply transitions from a $1/d^2$-dependence for small $l$ to a $1/d$-dependence for large $l$. Now focus on the two values of $\mu$ that we have adopted. Recall that evanescent modes are irrelevant when $\mu = 5$, and make no contribution to the time-dependent solution when $\mu = 1.5$. One therefore recognizes that only the second summation in Equation (28) matters. What results from Equation (28) when $d/R$ increases is then an increasingly refined discretization of some Fourier integral over a continuum of $\omega$ extending from $kv_{\mathrm{Ae}}$ to infinity. The relevant terms of this integral, applicable to a truly open system ($d/R \to \infty$), was explicitly worked out for $\mu = \infty$ by ORT15 (see Appendix A.1 for details). Evidently, one byproduct of our modal approach on a closed domain is the numerical distribution in the $\omega - r$ space of the terms in the Fourier integral, which cannot be expressed in closed-form for general $\mu$ to our knowledge.

Supposing $\Lambda/R$ is adjustable in view of Figure 5, we move on to demonstrate a generic condition for evanescent modes to be negligible. It suffices to adopt a truly open system, and consider the signal at a specific location such as $r = R$. We start with the assumption that evanescent modes do not contribute, and deduce the condition that ensures this assumption. Let $\tau$ denote the extent of the duration of interest, by which we mean that the signal becomes too weak to discern when

$t > \tau$. Evidently the outermost edge travels to a distance of $D_\tau$. Recall that the spatial extent of the eigenfunctions of the evanescent modes $D_l$ increases with $l$. One therefore deduces that evanescent modes are bound to be negligible when $D_\tau < D_1$. On the other hand, $D_\tau$ is evidently lower than $\Lambda + v_{\rm Ae}\tau$ because the speed at which the outermost edge travels ($v_{\rm A}(r)$) is consistently lower than $v_{\rm Ae}$. It then follows that evanescent modes can be neglected, provided

$$\Lambda + v_{\rm Ae}\tau < D_1. \tag{31}$$

Equating $\tau$ to $\tau_{\rm ener}$ in Figure 5, one readily finds that the inequality holds for all the values of $\Lambda$ examined therein, thereby explaining why the wave behavior is solely characterized by dispersive propagation but shows no sign of wave trapping. In fact, we can slightly generalize Equation (31) by supposing $\Lambda \gg R$ and adopting the worst-case scenario that $\tau$ is given by $t_{2+}$ in Equation (19). We further neglect the deviation of $v_{\rm A}(r)$ from $v_{\rm Ae}$, meaning that $t_{1-}(\Lambda/2 \to 0) \approx \Lambda/2v_{\rm Ae}$ and $t_{2+}(0 \to \Lambda) \approx \Lambda/v_{\rm Ae}$. A rather safe estimate for $t_{2+}$ and hence $\tau$ is then $3\Lambda/2v_{\rm Ae}$. The inequality (31) therefore becomes

$$\Lambda < \frac{2D_1}{5}. \tag{32}$$

Note that the RHS evaluates to $\sim 4000\,R$ in view of Figure 10, and further evaluates to $\sim 8\times10^6$ km if we quote an $R \sim 2000$ km from Figure 1 in Schrijver (2007) in keeping with the adopted $L/R = 15$. One therefore deduces that trapped modes are unlikely to be relevant in the temporal evolution of axial fundamental sausage modes in AR loops at least for the $[\rho_{\rm i}/\rho_{\rm e}, L/R]$ examined here. We stress that trapped modes are allowed as eigensolutions on an open system when $\mu < 2$ as pointed out by LN15. Likewise, we stress that their distinct dispersive behavior relative to trapped modes in the canonical ER83 equilibrium is relevant when large values of $k$ are involved such as happens for impulsive sausage wavetrains in AR loops. This latter point is clear if one contrasts Figure 8 with Figure 3 in Yu et al. (2017). It is just that the existence of trapped modes for $\mu < 2$ on an open system does not guarantee that they contribute to the temporal evolution of axial fundamentals.

## 5. SUMMARY

Focusing on fast sausage modes (FSMs) in solar coronal loops, this study aimed at examining the consequences of some peculiar dispersive properties that may arise in an equilibrium differing from Edwin & Roberts (1983, ER83) only by replacing the step with a continuous density profile ($\rho_0(r)$). By "peculiar" we mean that FSMs are not subject to cutoff axial wavenumbers when $\rho_0(r)$ outside the cylinder possesses a sufficiently shallow $r$-dependence, which was first recognized on firm mathematical grounds by Lopin & Nagorny (2015a, LN15) when analyzing the relevent eigenvalue problem (EVP) on a radially open system. Two effects follow. Firstly, FSMs may be trapped regardless of the axial wavenumber $k$ and the density contrast $\rho_{\rm i}/\rho_{\rm e}$. Secondly, long-wavelength trapped FSMs are nearly dispersionless with their axial phase speeds differing little from the external Alfvén speed. These two effects then led LN15 and Lopin & Nagorny (2019) to deduce that fast sausage perturbations of observable quality may exist in active region (AR) loops and flare loops alike, with their periodicities characterized by the longitudinal rather than the canonical transverse Alfvén time. If true, this deduction may substantially broaden the range of observed periodicities that FSMs can account for, and therefore offer more seismological possibilities.

We took efforts to make our scope as narrow as possible by addressing the question "does the existence of trapped modes in EVPs on an open system guarantee that they play a role in determining

the temporal behavior of sausage perturbations"? To be specific, we chose to work in the framework of linearized, pressureless, ideal MHD, and specialize to an "outer-$\mu$" density profile (Equation (17)). The solution to the relevant initial value problem on an open system (IVP 1) is then determined by the dimensionless parameters $[\rho_{\rm i}/\rho_{\rm e}, \mu; kR; \Lambda/R]$, where $\mu$ characterizes the steepness of the density profile outside the nominal radius $R$, and $\Lambda$ represents the spatial extent of the initial perturbation. We focus on axial fundamentals in AR loops by taking $[\rho_{\rm i}/\rho_{\rm e}, kR] = [2.25, \pi/15]$ in view of the observational constraints from EUV measurements (Aschwanden et al. 2004; Schrijver 2007). We distinguish between the cases with $\mu < 2$ and $\mu > 2$ because trapped modes are present (absent) in the former (latter) for the chosen $[\rho_{\rm i}/\rho_{\rm e}, kR]$. IVP 1 is solved with both a direct finite-difference (FD) approach and a modal approach whereby the solution is expressed as the superposition of eigenmodes for the pertinent EVP on a closed domain (EVP 1). The dimensionless domain size $d/R$ is involved in the latter approach, the evanescent modes in which are the counterparts of trapped modes on a truely open system. Our findings can be summarized as follows.

The answer to the question we laid out is "No". We came to this conclusion primarily because the FD solutions for a substantial range of $\mu$ and $\Lambda/R$ are consistently characterized by some dispersive propagation but show no sign of wave trapping (Figure 5). In particular, the solutions show a smooth transition when $\mu$ crosses the nominally critical value of two. With the modal approach, we showed that more and more evanescent modes appear when the domain size increases, thereby lending further support to the recognition of LN15. However, even the shortest spatial extent of the evanescent eigenfunctions is well beyond the observationally reasonable range of the spatial extent of initial perturbations [6]. Consequently, the initial perturbations cannot impart a discernible fraction of energy to evanescent modes, which in turn means that these modes do not contribute to the temporal evolution of the system.

Before closing, we offer some further remarks on the influence on coronal FSMs due to the deviation of the equilibrium from ER83. We start by noting that the formulation of the transverse structuring actually offers a mixed message for FSMs in terms of their observational applications. On the one hand, sausage-like perturbations are robust in the sense that they are permitted even when waveguides are not strictly axisymmetric as happens for waveguides with, say, elliptic (e.g., Erdélyi & Morton 2009; Aldhafeeri et al. 2021) or even irregular cross-sections (Aldhafeeri 2021; Guo et al. 2021). On the other hand, that the dispersive behavior of FSMs in non-ER83 equilibria may be qualitatively different does not necessarily mean that FSMs can be invoked to interpret a broader range of periodicities. That said, one cannot rule out coronal FSMs as an interpretation for oscillations with periodicities on the order of the longitudinal Alfvén time either. Let us name only one possible equilibrium configuration where essentially the only difference from ER83 is the introduction of a magnetically twisted boundary layer. Radial fundamental FSMs may be trapped regardless of the axial wavenumber (e.g., Khongorova et al. 2012; Lim et al. 2018), the corresponding eigenfunctions possessing spatial scales that do not far exceed the cylinder radius (e.g., Mikhalyaev & Bembitov 2014; Lopin 2021). One readily deduces that these radial fundamental FSMs may indeed show up in reality, even though a definitive answer relies on a detailed study from the IVP perspective.

[6] Some subtleties arise as a result of our outer-$\mu$ formulation. Further computations are therefore conducted, the descriptions of which are nonetheless collected in Appendix C to streamline the main text. Our conclusion remains valid, namely that the existence of trapped modes in EVPs on an open system does not necessarily mean that they can show up in the evolution of the system in response to sausage-type perturbations.

We thank the referee for constructive comments. This research was supported by the National Natural Science Foundation of China (41974200 and 11761141002). We gratefully acknowledge ISSI-BJ for supporting the workshop on "Oscillatory Processes in Solar and Stellar Coronae", during which this study was partly initiated.

## REFERENCES

Aldhafeeri, A. A. 2021, PhD thesis, University of Sheffield. https://etheses.whiterose.ac.uk/29022/

Aldhafeeri, A. A., Verth, G., Brevis, W., et al. 2021, ApJ, 912, 50, doi: 10.3847/1538-4357/abec7a

Andries, J., & Goossens, M. 2007, Physics of Plasmas, 14, 052101, doi: 10.1063/1.2714513

Anfinogentov, S. A., & Nakariakov, V. M. 2019, ApJL, 884, L40, doi: 10.3847/2041-8213/ab4792

Arregui, I. 2018, Advances in Space Research, 61, 655, doi: 10.1016/j.asr.2017.09.031

Arregui, I., & Goossens, M. 2019, A&A, 622, A44, doi: 10.1051/0004-6361/201833813

Aschwanden, M. J., Nakariakov, V. M., & Melnikov, V. F. 2004, ApJ, 600, 458, doi: 10.1086/379789

Aschwanden, M. J., Nightingale, R. W., Andries, J., Goossens, M., & Van Doorsselaere, T. 2003, ApJ, 598, 1375, doi: 10.1086/379104

Banerjee, D., Erdélyi, R., Oliver, R., & O'Shea, E. 2007, SoPh, 246, 3, doi: 10.1007/s11207-007-9029-z

Bender, C. M., & Orszag, S. A. 1999, Advanced mathematical methods for scientists and engineers: I: Asymptotic methods and perturbation theory (Springer)

Berghmans, D., de Bruyne, P., & Goossens, M. 1996, ApJ, 472, 398, doi: 10.1086/178072

Cally, P. S. 1986, SoPh, 103, 277, doi: 10.1007/BF00147830

Chen, S.-X., Li, B., Xiong, M., Yu, H., & Guo, M.-Z. 2015, ApJ, 812, 22, doi: 10.1088/0004-637X/812/1/22

—. 2016, ApJ, 833, 114, doi: 10.3847/1538-4357/833/1/114

De Moortel, I., & Nakariakov, V. M. 2012, Philosophical Transactions of the Royal Society of London Series A, 370, 3193, doi: 10.1098/rsta.2011.0640

Edwin, P. M., & Roberts, B. 1983, SoPh, 88, 179, doi: 10.1007/BF00196186

Edwin, P. M., & Roberts, B. 1986, in NASA Conference Publication, Vol. 2449, NASA Conference Publication, 347–357

Erdélyi, R., & Morton, R. J. 2009, A&A, 494, 295, doi: 10.1051/0004-6361:200810318

Goddard, C. R., Pascoe, D. J., Anfinogentov, S., & Nakariakov, V. M. 2017, A&A, 605, A65, doi: 10.1051/0004-6361/201731023

Goossens, M., Andries, J., Soler, R., et al. 2012, ApJ, 753, 111, doi: 10.1088/0004-637X/753/2/111

Goossens, M., Terradas, J., Andries, J., Arregui, I., & Ballester, J. L. 2009, A&A, 503, 213, doi: 10.1051/0004-6361/200912399

Guo, M., Li, B., & Shi, M. 2021, ApJL, 921, L17, doi: 10.3847/2041-8213/ac30e3

Guo, M., Li, B., & Van Doorsselaere, T. 2020, ApJ, 904, 116, doi: 10.3847/1538-4357/abc1df

Guo, M.-Z., Chen, S.-X., Li, B., Xia, L.-D., & Yu, H. 2016, SoPh, 291, 877, doi: 10.1007/s11207-016-0868-3

Hood, A. W., Ruderman, M., Pascoe, D. J., et al. 2013, A&A, 551, A39, doi: 10.1051/0004-6361/201220617

Jelínek, P., & Karlický, M. 2012, A&A, 537, A46, doi: 10.1051/0004-6361/201117883

Karlický, M., Jelínek, P., & Mészárosová, H. 2011, A&A, 529, A96, doi: 10.1051/0004-6361/201016171

Katsiyannis, A. C., Williams, D. R., McAteer, R. T. J., et al. 2003, A&A, 406, 709, doi: 10.1051/0004-6361:20030458

Khongorova, O. V., Mikhalyaev, B. B., & Ruderman, M. S. 2012, SoPh, 280, 153, doi: 10.1007/s11207-012-0056-z

Kolotkov, D. Y., Nakariakov, V. M., Moss, G., & Shellard, P. 2021, MNRAS, 505, 3505, doi: 10.1093/mnras/stab1587

Kopylova, Y. G., Melnikov, A. V., Stepanov, A. V., Tsap, Y. T., & Goldvarg, T. B. 2007, Astronomy Letters, 33, 706, doi: 10.1134/S1063773707100088
Kupriyanova, E. G., Melnikov, V. F., & Shibasaki, K. 2013, SoPh, 284, 559, doi: 10.1007/s11207-012-0141-3
Li, B., Antolin, P., Guo, M. Z., et al. 2020, SSRv, 216, 136, doi: 10.1007/s11214-020-00761-z
Li, B., Guo, M.-Z., Yu, H., & Chen, S.-X. 2018, ApJ, 855, 53, doi: 10.3847/1538-4357/aaaf19
Lim, D., Nakariakov, V. M., & Moon, Y.-J. 2018, Journal of Atmospheric and Solar-Terrestrial Physics, 175, 49, doi: 10.1016/j.jastp.2018.04.013
Lim, D., Nakariakov, V. M., Yu, D. J., Cho, I.-H., & Moon, Y.-J. 2020, ApJ, 893, 62, doi: 10.3847/1538-4357/ab7d3d
Lopin, I., & Nagorny, I. 2015a, ApJ, 810, 87, doi: 10.1088/0004-637X/810/2/87
—. 2015b, ApJ, 801, 23, doi: 10.1088/0004-637X/801/1/23
—. 2019, MNRAS, 488, 660, doi: 10.1093/mnras/stz1737
Lopin, I. P. 2021, MNRAS, 505, 1878, doi: 10.1093/mnras/stab1355
McLaughlin, J. A., Nakariakov, V. M., Dominique, M., Jelínek, P., & Takasao, S. 2018, SSRv, 214, 45, doi: 10.1007/s11214-018-0478-5
Meerson, B. I., Sasorov, P. V., & Stepanov, A. V. 1978, SoPh, 58, 165, doi: 10.1007/BF00152562
Mikhalyaev, B. B., & Bembitov, D. B. 2014, SoPh, 289, 4069, doi: 10.1007/s11207-014-0566-y
Murawski, K., & Roberts, B. 1993, SoPh, 144, 101, doi: 10.1007/BF00667986
Nakariakov, V. M., Arber, T. D., Ault, C. E., et al. 2004, MNRAS, 349, 705, doi: 10.1111/j.1365-2966.2004.07537.x
Nakariakov, V. M., Hornsey, C., & Melnikov, V. F. 2012, ApJ, 761, 134, doi: 10.1088/0004-637X/761/2/134
Nakariakov, V. M., & Kolotkov, D. Y. 2020, ARA&A, 58, 441, doi: 10.1146/annurev-astro-032320-042940
Nakariakov, V. M., & Verwichte, E. 2005, Living Reviews in Solar Physics, 2, 3, doi: 10.12942/lrsp-2005-3
Nakariakov, V. M., Pilipenko, V., Heilig, B., et al. 2016, SSRv, 200, 75, doi: 10.1007/s11214-015-0233-0
Nakariakov, V. M., Anfinogentov, S. A., Antolin, P., et al. 2021, SSRv, 217, 73, doi: 10.1007/s11214-021-00847-2
Nechaeva, A., Zimovets, I. V., Nakariakov, V. M., & Goddard, C. R. 2019, ApJS, 241, 31, doi: 10.3847/1538-4365/ab0e86
Oliver, R., Ruderman, M. S., & Terradas, J. 2014, ApJ, 789, 48, doi: 10.1088/0004-637X/789/1/48
—. 2015, ApJ, 806, 56, doi: 10.1088/0004-637X/806/1/56
Pascoe, D. J., Anfinogentov, S. A., Goddard, C. R., & Nakariakov, V. M. 2018, ApJ, 860, 31, doi: 10.3847/1538-4357/aac2bc
Pascoe, D. J., Goddard, C. R., Nisticò, G., Anfinogentov, S., & Nakariakov, V. M. 2016, A&A, 585, L6, doi: 10.1051/0004-6361/201527835
Pascoe, D. J., & Nakariakov, V. M. 2016, A&A, 593, A52, doi: 10.1051/0004-6361/201526546
Pascoe, D. J., Nakariakov, V. M., Arber, T. D., & Murawski, K. 2009, A&A, 494, 1119, doi: 10.1051/0004-6361:200810541
Pascoe, D. J., Nakariakov, V. M., & Kupriyanova, E. G. 2013, A&A, 560, A97, doi: 10.1051/0004-6361/201322678
Roberts, B. 2008, in Waves & Oscillations in the Solar Atmosphere: Heating and Magneto-Seismology, ed. R. Erdélyi & C. A. Mendoza-Briceno, Vol. 247, 3–19, doi: 10.1017/S1743921308014609
Roberts, B. 2019, MHD Waves in the Solar Atmosphere (Cambridge University Press), doi: 10.1017/9781108613774
Roberts, B., Edwin, P. M., & Benz, A. O. 1983, Nature, 305, 688, doi: 10.1038/305688a0
—. 1984, ApJ, 279, 857, doi: 10.1086/161956
Ruderman, M. S., & Terradas, J. 2013, A&A, 555, A27, doi: 10.1051/0004-6361/201220195
Samanta, T., Singh, J., Sindhuja, G., & Banerjee, D. 2016, SoPh, 291, 155, doi: 10.1007/s11207-015-0821-x
Schrijver, C. J. 2007, ApJL, 662, L119, doi: 10.1086/519455
Sewell, G. 1988, The Numerical Solution of Ordinary and Partial Differential Equations (San Diego: Academic Press)
Shestov, S., Nakariakov, V. M., & Kuzin, S. 2015, ApJ, 814, 135, doi: 10.1088/0004-637X/814/2/135

Spruit, H. C. 1982, SoPh, 75, 3, doi: 10.1007/BF00153456
Su, J. T., Shen, Y. D., Liu, Y., Liu, Y., & Mao, X. J. 2012, ApJ, 755, 113, doi: 10.1088/0004-637X/755/2/113
Terradas, J., Andries, J., & Goossens, M. 2007, SoPh, 246, 231, doi: 10.1007/s11207-007-9067-6
Terradas, J., Oliver, R., & Ballester, J. L. 2006, ApJ, 642, 533, doi: 10.1086/500730
Tian, H., Young, P. R., Reeves, K. K., et al. 2016, ApJL, 823, L16, doi: 10.3847/2041-8205/823/1/L16
Vasheghani Farahani, S., Hornsey, C., Van Doorsselaere, T., & Goossens, M. 2014, ApJ, 781, 92, doi: 10.1088/0004-637X/781/2/92
Wang, T., Ofman, L., Yuan, D., et al. 2021, SSRv, 217, 34, doi: 10.1007/s11214-021-00811-0
Wang, T. J. 2016, Washington DC American Geophysical Union Geophysical Monograph Series, 216, 395, doi: 10.1002/9781119055006.ch23
Wentzel, D. G. 1979, A&A, 76, 20
Williams, D. R., Mathioudakis, M., Gallagher, P. T., et al. 2002, MNRAS, 336, 747, doi: 10.1046/j.1365-8711.2002.05764.x
Yang, Z., Bethge, C., Tian, H., et al. 2020, Science, 369, 694, doi: 10.1126/science.abb4462
Yu, H., Li, B., Chen, S.-X., Xiong, M., & Guo, M.-Z. 2016a, ApJ, 833, 51, doi: 10.3847/1538-4357/833/1/51
—. 2017, ApJ, 836, 1, doi: 10.3847/1538-4357/836/1/1
Yu, S., Nakariakov, V. M., & Yan, Y. 2016b, ApJ, 826, 78, doi: 10.3847/0004-637X/826/1/78
Zajtsev, V. V., & Stepanov, A. V. 1975, Issledovaniia Geomagnetizmu Aeronomii i Fizike Solntsa, 37, 3
Zimovets, I. V., & Nakariakov, V. M. 2015, A&A, 577, A4, doi: 10.1051/0004-6361/201424960
Zimovets, I. V., McLaughlin, J. A., Srivastava, A. K., et al. 2021, SSRv, 217, 66, doi: 10.1007/s11214-021-00840-9

# APPENDIX

## A. STANDING SAUSAGE MODES IN CORONAL CYLINDERS WITH STEP PROFILES

### A.1. *Solution to IVP 1 in Terms of Eigenmods for an Open System*

This subsection presents the formal solution to IVP 1 expressed as the superposition of eigenmodes for a laterally unbounded system. We closely follow the Fourier-integral-based approach that ORT15 adopted to examine the two-dimensional (2D) propagation of sausage wavetrains in a system that is unbounded in the axial direction as well. The modal solution to our IVP 1 is actually part of their 2D solution. Consequently, only slight revisions to Equation (25) in ORT15 are needed to ensure dimensional and notational consistency. We choose to provide a minimal set of equations leading to the modal solution for two reasons. One, some equations will find immediate applications to the pertinent EVP on a closed domain. Two, the conceptual understanding embedded in the formal solution to IVP 1 should be informative for future studies on standing sausage perturbations in generic coronal structures. To this end, we see the axial wavenumber ($k$) as given and arbitrary.

The following notations are necessary. We use $J_n$ and $Y_n$ to represent Bessel functions of the first and second kind, respectively. Likewise, $I_n$ and $K_n$ denote modified Bessel functions of the first and second kind, respectively. Only orders $n = 0$ and 1 are relevant. In particular, $j_{n,m}$ denotes the $m$-th zero of $J_n$ with $m = 1, 2, \cdots$. The cutoff wavenumbers are then given by

$$k_{\rm cutoff,m} R = \frac{j_{0,m}}{\sqrt{\rho_{\rm i}/\rho_{\rm e} - 1}}. \tag{A1}$$

Defining

$$\begin{aligned} k_{\rm i}^2 &= \frac{\omega^2 - k^2 v_{\rm Ai}^2}{v_{\rm Ai}^2}, \\ k_{\rm e}^2 &= \frac{\omega^2 - k^2 v_{\rm Ae}^2}{v_{\rm Ae}^2}, \\ \kappa_{\rm e}^2 &= -\frac{\omega^2 - k^2 v_{\rm Ae}^2}{v_{\rm Ae}^2} = -k_{\rm e}^2, \end{aligned} \tag{A2}$$

we note that $\omega$ always exceeds $k v_{\rm Ai}$ and hence $k_{\rm i}^2$ are always positive.

The modal solution to IVP 1 involves both proper and improper modes, which are discriminated by the sign of $k_{\rm e}^2$. Proper modes ($k_{\rm e}^2 < 0$) are relevant when $k$ exceeds $k_{\rm cutoff,1}$, and correspond to a discrete set of frequencies. Let $j$ label a proper mode. Its eigenfunction reads

$$\breve{v}_j(r) = \begin{cases} -\dfrac{v_{\rm Ai}}{k_{\rm i} R} K_0(\kappa_{\rm e} R) J_1(k_{\rm i} r), & 0 \le r \le R, \\ \dfrac{v_{\rm Ai}}{\kappa_{\rm e} R} J_0(k_{\rm i} R) K_1(\kappa_{\rm e} r), & r > R. \end{cases} \tag{A3}$$

Written in this form, Equation (A3) ensures that $d\breve{v}_j(r)/dr$ is continuous. The mode frequency is then dictated by the continuity of $\breve{v}_j$ itself across $r = R$, which leads to the well-known dispersion relation (DR, e.g., ER83; also Meerson et al. 1978; Spruit 1982; Cally 1986)

$$k_{\rm i} \frac{J_0(k_{\rm i} R)}{J_1(k_{\rm i} R)} + \kappa_{\rm e} \frac{K_0(\kappa_{\rm e} R)}{K_1(\kappa_{\rm e} R)} = 0 \ . \tag{A4}$$

Improper modes ($k_{\rm e}^2 > 0$) are relevant regardless of $k$, their frequencies continuously spanning the range $(kv_{\rm Ae}, \infty)$. The eigenfunction reads

$$\breve{v}_\omega(r) = \begin{cases} -v_{\rm Ai}\dfrac{k_{\rm e}^2 R}{k_{\rm i}} J_1(k_{\rm i} r), & 0 \le r \le R, \\ -v_{\rm Ai}(k_{\rm e}R)\left[C_J J_1(k_{\rm e} r) + C_Y Y_1(k_{\rm e} r)\right], & r > R, \end{cases} \tag{A5}$$

where

$$\begin{aligned} C_J &= \frac{\pi k_{\rm e} R}{2k_{\rm i}}\left[-k_{\rm i} J_0(k_{\rm i}R) Y_1(k_{\rm e}R) + k_{\rm e} J_1(k_{\rm i}R) Y_0(k_{\rm e}R)\right], \\ C_Y &= \frac{\pi k_{\rm e} R}{2k_{\rm i}}\left[-k_{\rm e} J_1(k_{\rm i}R) J_0(k_{\rm e}R) + k_{\rm i} J_0(k_{\rm i}R) J_1(k_{\rm e}R)\right]. \end{aligned} \tag{A6}$$

Both $\breve{v}_\omega$ and $d\breve{v}_\omega(r)/dr$ are ensured to be continuous. The modal solution eventually reads

$$\begin{aligned} &\hat{v}(r,t) = \sum_{j=1}^{J} c_j \breve{v}_j(r)\cos(\omega_j t) + \int_{kv_{\rm Ae}}^{\infty} S_\omega \breve{v}_\omega(r)\cos(\omega t) d\omega, \\ &0 < r < \infty, \quad 0 < t < \infty, \end{aligned} \tag{A7}$$

where

$$\begin{aligned} c_j &= \frac{\displaystyle\int_0^\infty u(r)\breve{v}_j(r)\rho_0(r) r dr}{\displaystyle\int_0^\infty \breve{v}_j^2(r)\rho_0(r) r dr}, \\ S_\omega &= \frac{\omega \displaystyle\int_0^\infty u(r)\breve{v}_\omega(r)\rho_0(r) r dr}{(\rho_{\rm e} v_{\rm Ai}^2 R^2)(k_{\rm e} v_{\rm Ae})^2 (C_J^2 + C_Y^2)}. \end{aligned} \tag{A8}$$

Let us summarize the steps to solve IVP 1 given $\rho_{\rm i}/\rho_{\rm e}$, $k$, and $u(r)$. First of all, with Equation (A1) one counts $J$, the number of cutoff wavenumbers that are smaller than $k$. Evidently, $J = 0$ if $k < k_{\rm cutoff,1}$, making proper modes irrelevant. Secondly, if $J \ge 1$, then for each allowed $j$ one evaluates its eigenfrequency $\omega_j$ and then its eigenfunction $\breve{v}_j$ with Equations (A4) and (A3), respectively. The contribution of the proper mode, $c_j$, can then be found with Equation (A8). Thirdly, with Equations (A5) and (A6) one evaluates the improper eigenfunction for any $\omega > kv_{\rm Ae}$. The contribution from the improper mode, $S_\omega$, is then readily found with Equation (A8).

### A.2. *Eigenmodes for a Closed System*

This subsection examines some properties of the eigenmodes for a closed system, namely the solutions to EVP 1 specialized to a step density profile. We start with a concrete example found for $[\rho_{\rm i}/\rho_{\rm e}, kR] = [2.25, \pi/15]$ and an initial perturbation given by Equation (18) with $\Lambda/R = 4$. IVP 1 is solved with three independent methods. The first, to be called "modal open", is based on eigenmodes on an open system, whereas the second ("modal closed") is based on Equation (23) for a domain size $d = 50\ R$. The two sets of solutions agree exactly with each other, and further agree with the

solution found with the simpler finite-difference approach. We choose not to present the comparison among the time-dependent solutions, because a comparison between the frequency-dependencies of the modal contributions seems more informative but is unavailable as far as we know. Note that these contributions for the chosen $[\rho_{\rm i}/\rho_{\rm e}, kR]$ are solely due to improper (oscillatory) modes in the "modal open" ("modal closed") approach. With Equations (28) and (A8) in mind, Figure 11 then specializes to $r = R$ and compares the local spectral density $S_l\breve{v}_l(R)$ from the "modal closed" approach (the asterisks) with $S_\omega\breve{v}_\omega(R)$ from the "modal open" approach (the blue solid curve). It is reassuring to see that the solid curve threads exactly the symbols, meaning that the continuum of improper modes is adequately resolved by the discrete oscillatory modes despite the rather modest domain size.

We now focus on the discrete modes themselves by recalling the discussions immediately following Equation (26). Firstly, $k_{\rm i}^2 > 0$ is guaranteed because $\omega_l$ necessarily exceeds $kv_{\rm Ai}$. Secondly, the mode classification is eventually determined by how $\omega_l$ compares with $kv_{\rm Ae}$, meaning that $k_{\rm e}^2$ is positive (negative) when a mode is oscillatory (evanescent). Regardless, the eigenfunction $\breve{v}_l(r)$ can be consistently described by Equation (A5), the reason being that $J_1(k_{\rm e}r)$ and $Y_1(k_{\rm e}r)$ always form a numerically satisfactory pair in the outer region $(R < r < d)$ [7]. The requirement $\breve{v}_l(r = d) = 0$ then gives a DR that governs the mode frequency $\omega_l$,

$$C_J J_1(k_{\rm e}d) + C_Y Y_1(k_{\rm e}d) = 0. \tag{A9}$$

We now specialize to the situation where $k < k_{\rm cutoff,1}$ to better connect with the main text, the associated analytical progress being new to our knowledge.

Let us examine the analytical behavior of the modes with frequencies $\omega_l$ just above $\omega_{\rm crit} = kv_{\rm Ae}$. Expressing $\omega_l$ as $kv_{\rm Ae}(1 + \delta)$ with $0 < \delta \ll 1$, one finds that $k_{\rm i}^2 \approx k^2(\rho_{\rm i}/\rho_{\rm e} - 1)$ and $k_{\rm e}^2 \approx k^2(2\delta)$ (see Equation (A2)). Now suppose that $k_{\rm e}R \ll 1$. The approximate expressions of $J_n$ and $Y_n$ for small arguments then indicate that $Y_1(k_{\rm e}R) \sim 1/(k_{\rm e}R)$ is the most singular term in the coefficients $C_J$ and $C_Y$ (see Equation (A6)). The left-hand side (LHS) of the DR (A9) is therefore dominated by the first term, meaning that $k_{\rm e}d \approx j_{1,l}$. In other words,

$$\delta = \frac{\omega_l}{kv_{\rm Ae}} - 1 \approx \frac{j_{1,l}^2}{2(kd)^2}. \tag{A10}$$

Given the assumptions $\delta \ll 1$ and $k_{\rm e}R \ll 1$, the modes in question are characterized by

$$\frac{\omega_l}{kv_{\rm Ae}} \approx 1 + \frac{j_{1,l}^2}{2(kd)^2}, \quad \text{provided } d/R \gg j_{1,l}, \quad (kd)^2 \gg j_{1,l}^2. \tag{A11}$$

Now consider high-frequency modes in a system with $d/R \gg 1$. By "high" we assume that

$$\omega_l \gg v_{\rm Ae}/R, \quad \omega_l \gg kv_{\rm Ae}. \tag{A12}$$

It then follows from Equation (A2) that $k_{\rm i}R, k_{\rm e}R \gg 1$ and hence $k_{\rm i}d, k_{\rm e}d \gg 1$. With the expressions for $J_n$ and $Y_n$ at large arguments, some algebra indicates that the DR (A9) approximates to

$$\sin[k_{\rm e}(d - R) + \phi_{\rm e}] = 0, \tag{A13}$$

[7] The outer solution can be equivalently expressed by the numerically satisfactory pair $I_1(\kappa_{\rm e}r)$ and $K_1(\kappa_{\rm e}r)$ (see BDBG96, for details). It is just that $\kappa_{\rm e}^2$ is positive (negative) for evanescent (oscillatory) modes.

where $\phi_{\rm e}$ satisfies the relation

$$\tan\phi_{\rm e} = \sqrt{\rho_{\rm e}/\rho_{\rm i}}\tan\left[\sqrt{\rho_{\rm i}/\rho_{\rm e}}(k_{\rm e}R) - \frac{\pi}{4}\right]. \tag{A14}$$

Note that Equation (A13) is implicit in $\omega_l$ because $\omega_l$ is involved in Equation (A14). Note further that the range of $\phi_{\rm e}$ is not restricted by Equation (A14) per se. However, as can be verified a posteriori, $\phi_{\rm e}$ is negligible to leading order, meaning that $k_{\rm e} \approx l\pi/(d-R) \approx l\pi/d$. If desired, this solution can be plugged into Equation (A14) to yield the first-order correction due to $\phi_{\rm e}$, resulting in

$$\omega_l \approx (l\pi - \phi_l)\,\frac{v_{\rm Ae}}{d-R}. \tag{A15}$$

Here $\phi_l$ given by

$$\phi_l = \arctan\left[\sqrt{\rho_{\rm e}/\rho_{\rm i}}\tan\left(\sqrt{\rho_{\rm i}/\rho_{\rm e}}\frac{l\pi}{d/R-1} - \frac{\pi}{4}\right)\right] + \left\lfloor\sqrt{\rho_{\rm i}/\rho_{\rm e}}\frac{l}{d/R-1} + \frac{1}{4}\right\rfloor\pi, \tag{A16}$$

with the floor function $\lfloor\cdot\rfloor$ introduced to make $\phi_l$ continuous with respect to $l$. Restricting oneself to those modes with $l \gg d/(\pi R)$ and $l \gg kd/\pi$ in view of the assumptions (A12), one recognizes that the RHS of Equation (A16) is necessarily far smaller than $l\pi$. Overall, it suffices for our purposes to summarize the properties of the high-frequency modes as

$$\omega_l \approx l\pi(v_{\rm Ae}/d), \quad \text{for } l \gg \frac{d/R}{\pi}, \quad l \gg \frac{kd}{\pi}. \tag{A17}$$

## B. SOME FURTHER PROPERTIES OF EVP 1

This section examines some further properties of EVP 1 by capitalizing on the Schrödinger Equation (26). We recall that the equilibrium density is of the "outer-$\mu$" type (see Equation (17)). This subsection extends Subsection A.2 in that $\mu$ is no longer restricted to be infinite.

We start by showing that all solutions to EVP 1 necessarily possess an $\omega_l$ that exceeds $kv_{\rm Ai}$, regardless of $\mu$ or $d/R$. What we offer is only a slight generalization of the arguments given by BDBG96 for a step density profile. This generalization is possible because the arguments therein rely only on two conditions, one being that the potential $V(r)$ consistently exceeds $k^2v_{\rm Ai}^2$, and the other being that the eigenfunction $\breve{v}_l(r)$ vanishes at both $r=0$ and $r=d$. Neither condition is restricted to the particular $\mu=\infty$. Now suppose that $\omega_l < kv_{\rm Ai}$ for some mode, meaning that $\omega_l^2 < V(r)$. The wavefunction $\Phi(r)$ and hence the eigenfunction $\breve{v}_l(r)$ then necessarily peak somewhere in the domain, diminishing toward both smaller and larger $r$. One then deduces that $d\breve{v}_l(r)/dr$ is discontinuous, thereby violating the continuity requirement for the Eulerian perturbation of total pressure.

We now address high-frequency modes in a system with $d/R \gg 1$, "high" in the same sense as in the assumption (A12). Our approach is essentially a classical WKB one detailed in Bender & Orszag (1999, Chapter 10). Somehow different is that we avoid the complication associated with the turning points (namely where $V(r)=0$), which are bound to occur at small $r$ for high-frequency modes because $V(r)$ diverges at $r=0$. This is done by handling the Schrödinger Equation (26) in the interior ($r<R$) and exterior ($r>R$) separately. First consider the exterior, where the condition $\omega^2 \gg V(r)$ is ensured by Equation (A12). The leading order WKB solution to Equation (26) reads

$$\Phi(r) \approx A_{\rm e}v_{\rm A}^{1/2}(r)\sin[\Theta(r)], \tag{B18}$$

where

$$\Theta(r) = \omega \int_R^r \frac{dr'}{v_{\rm A}(r')} + \phi$$

with $A_{\rm e}$ and $\phi$ being constants. Requiring $\Phi(d) = 0$ then leads to

$$\omega_l \approx \frac{l\pi - \phi_l}{\int_R^d dr'/v_{\rm A}(r')} \tag{B19}$$

for mode $l$. Evidently, the integral in Equation (B19) is well approximated by $d/v_{\rm Ae}$ for large $d/R$. The high-frequency modes are therefore still characterized by Equation (A17), provided $|\phi_l| \ll l\pi$.

We proceed to show that the inequality $|\phi_l| \ll l\pi$ indeed holds via three mutually complementary methods. Firstly, we numerically solve EVP 1 for a substantial number of combinations of $[\rho_{\rm i}/\rho_{\rm e}, \mu; k; d/R]$. Comparing the computed $\omega_l$ with the RHS of Equation (B19) then indicates that $|\phi_l| \ll l\pi$. Secondly, we make some analytical progress to estimate $\phi_l$. Now the interior ($r < R$) needs to be examined, for which purpose Equation (A5) indicates that the exact solution to Equation (26) reads $\Phi(r) = A_{\rm i} r^{1/2} J_1(k_{\rm i} r)$ with $A_{\rm i}$ being an arbitrary constant. In addition, the condition $k_{\rm i} R \gg 1$ is ensured by the assumption (A12), enabling one to employ the approximate expressions for Bessel functions at large arguments to find

$$\left.\frac{d\Phi/dr}{\Phi}\right|_{r=R^-} \approx k_{\rm i} \cot\left(k_{\rm i} R - \pi/4\right) - \frac{1}{2R}. \tag{B20}$$

One further finds with the external WKB solution (B18) that

$$\left.\frac{d\Phi/dr}{\Phi}\right|_{r=R^+} \approx k_{\rm i} \cot\phi_l + \frac{1}{2}\left.\frac{d\ln v_{\rm A}}{dr}\right|_{r=R^+}. \tag{B21}$$

Equating Equations (B20) to (B21) then leads to that

$$\cot\phi_l \approx \cot\left(k_{\rm i} R - \pi/4\right) - \frac{1}{2}\left(\frac{1}{k_{\rm i} R} + \frac{1}{k_{\rm i}}\left.\frac{d\ln v_{\rm A}}{dr}\right|_{r=R^+}\right). \tag{B22}$$

Now suppose that the second term in the RHS of Equation (B22) is negligible, implying that $\mu$ is not too large. Let us further see the RHS of Equation (B22) as known from Equation (A17). It turns out that $\phi_l$ can be approximated to leading order by $\phi_l \approx k_{\rm i} R - \pi/4 \approx l\pi\sqrt{\rho_{\rm i}/\rho_{\rm e}}/(d/R)$, meaning that $|\phi_l| \ll l\pi$ for sufficiently large $d/R$. Thirdly, we offer some heuristic arguments to estimate $|\phi_l|$ for arbitrary $\mu > 1$. Let $N_{\rm int}$ ($N_{\rm ext}$) be the the number of extrema in the eigenfunction $\breve{v}_l(r)$ in the interior $r < R$ (the exterior $R < r < d$). Evidently, $\phi_l$ in Equation (B19) stems from the influence of the interior, making $|\phi_l/\pi|/l$ essentially a measure of $N_{\rm int}/N_{\rm ext}$. With $d/R \gg 1$, one readily deduces that $N_{\rm int} \ll N_{\rm ext}$ and hence $|\phi_l| \ll l\pi$.

## C. INTRICACIES ASSOCIATED WITH THE "OUTER $\mu$" FORMULATION

This section examines some subtlety associated with our "outer $\mu$" formulation (17) for the equilibrium density $\rho_0(r)$. Let us recall our argument that, for the the fixed pair $[\rho_{\rm i}/\rho_{\rm e}, L/R] = [2.25, 15]$ and some chosen $\mu < 2$, the dimensionless spatial extent of the initial perturbation ($\Lambda/R$) needs to be unrealistically large for evanescent modes to be non-negligible in the time-dependent solutions to

IVP 1. However, Equation (17) indicates that the spatial range containing the density enhancement broadens when $\mu$ decreases, making the nominal radius $R$ less and less ideal for characterizing the spatial variation of $\rho_0(r)$. Let the spatial scale of $\rho_0(r)$ be measured by some effective radius $R_{\rm eff}$. One may question whether our argument still holds because there may be a regime where evanescent modes are visible for not so extreme values of $\Lambda$ measured in units of $R_{\rm eff}$ rather than $R$. Somehow it is non-trivial to quantify this aspect in an exhaustive manner, to explain which we note that we will exclusively adopt the FD approach to solve IVP 1 here for computational convenience. We will additionally fix the steepness parameter at $\mu = 1.5$, but experiment with two different values for the density contrast $\rho_{\rm i}/\rho_{\rm e}$. Let $\tau$ denote the duration to be examined in an FD solution, and $D_\tau$ the distance that the outer edge of the perturbation reaches when $t = \tau$. For now consider the modal structure for EVP 1 on a sufficiently large domain of size $d$, where by "sufficiently large" we mean that $d \gg D_\tau$ such that a multitude of evanescent modes exist. From Section 4 we know that oscillatory modes are always permitted, and the frequencies of evanescent modes ($\omega < \omega_{\rm crit} = kv_{\rm Ae}$) may not differ much from those of the low-frequency oscillatory modes ($\omega \gtrsim \omega_{\rm crit}$). Now that low-frequency oscillatory modes are excited in general, it may take some considerable amount of time for them to interfere such that their contribution to a time-dependent solution eventually becomes sufficiently weak to make evanescent modes visible. In practice, however, the value of $\tau$ cannot be made infinite. Three regimes then arise in the signal behavior within a large but nonetheless finite timeframe, where evanescent modes are not discernible, somehow discernible but weak, and stronger than some threshold, respectively. We see evanescent modes as observationally relevant only when the last regime occurs.

Some definitions and remarks are necessary here. We define $R_{\rm eff}$ as the radial distance where the function $f(r)$ in Equation (17) attains 1/10, a factor that is meant to be small but admittedly arbitrary. One nonetheless finds that $R_{\rm eff}/R = 10^{1/\mu}$ and evaluates to 4.64 for $\mu = 1.5$. We see $R_{\rm eff}$ rather than $R$ as being observationally relevant and consistently use $R_{\rm eff}$ to measure $\Lambda$ and the loop length $L$. Likewise, time will be measured in units of the longitudinal Alfvén time $\tau_{\rm long} = 2\pi/\omega_{\rm crit} = 2L/v_{\rm Ae}$, which is more relevant for the large-time behavior. We examine only the timeframe $t \lesssim 40\tau_{\rm long}$, which is seen as sufficiently long. Overall, the time-dependent solutions to IVP 1 are determined by the set of dimensionless parameters $[\rho_{\rm i}/\rho_{\rm e}, L/R_{\rm eff}, \Lambda/R_{\rm eff}]$ given a fixed $\mu = 1.5$. We deem the range $\Lambda/R_{\rm eff} \leq 20$ as observationally realistic for initial perturbations. On the other hand, we will examine the following two quantities to assess the significance of evanescent modes. The first is $\Gamma(t) = E_{\rm tot}(R_{\rm eff}, t)/E_0$ with $E_0 = E_{\rm tot}(\Lambda, t = 0)$ being the total energy initially deposited to the entire system. The second is simply the instantaneous radial speed at the effective radius $\hat{v}(R_{\rm eff}, t)$. While both $\Gamma(t)$ and $\hat{v}(R_{\rm eff}, t)$ measure the signal strength in the volume $r \leq R_{\rm eff}$, we find that the former can better bring out the differences when $L/R_{\rm eff}$ or $\Lambda/R_{\rm eff}$ varies.

We start by examining an AR loop with $[\rho_{\rm i}/\rho_{\rm e}, L/R_{\rm eff}] = [10, 10]$, which is only marginally realistic because in general $\rho_{\rm i}/\rho_{\rm e}$ ($L/R_{\rm eff}$) is lower (larger) in observations (e.g., Aschwanden et al. 2004; Schrijver 2007). Figure 12 displays the temporal profiles of (a) $\Gamma(t)$ and (b) $\hat{v}(R_{\rm eff}, t)$ for a number of $\Lambda/R_{\rm eff}$ as labeled. Examining any $\Lambda/R_{\rm eff}$ in the chosen timeframe, one sees that a periodic behavior develops at large $t$ for $\Gamma(t)$ and $\hat{v}(R_{\rm eff}, t)$ alike. We will focus on this periodic stage here and hereafter. A slight difference between Figures 12a and 12b is then that the period in $\Gamma(t)$ is half that in $\hat{v}(R_{\rm eff}, t)$, which arises simply because $E_{\rm tot}$ involves the perturbations as squared terms by definition (see Equation (12)). More importantly, the signal strengthens when $\Lambda/R_{\rm eff}$ increases

as can be discerned in Figure 12b and seen more clearly in Figure 12a. Regardless, the signal for any $\Lambda/R_{\rm eff}$ weakens monotonically with time, eventually resulting in extremely small values for both $\Gamma(t)$ and $\hat{v}(R_{\rm eff}, t)$. Note that this is true even for $\Lambda/R_{\rm eff} = 40$, which exceeds the range that we deem observationally realistic. Note further that the signal in the periodic stage tends to weaken when $L/R_{\rm eff}$ increases or $\rho_{\rm i}/\rho_{\rm e}$ decreases from the value we choose. Figure 12 therefore means that evanescent modes are not discernible for realistic combinations of $[\rho_{\rm i}/\rho_{\rm e}, L/R_{\rm eff}]$, thereby strengthening our conclusion that the existence of evanescent modes in the pertinent EVP analysis does not guarantee their relevance in the temporal evolution of the system. It then follows that one needs to invoke, say, kink modes, to account for a periodicity on the order of the longitudinal Alfvén time when analyzing oscillating AR loops even given our outer-$\mu$ formulation. Furthermore, whether an interpretation in terms of kink modes is justifiable can be readily assessed by looking for the tell-tale signature of transverse displacements because AR loops tend to be imaged with high spatial resolution on a routine basis.

That said, evanescent modes may indeed be discernible or visible if one experiments with, say, drastically different values of $\rho_{\rm i}/\rho_{\rm e}$. We proceed with a fixed combination $[\rho_{\rm i}/\rho_{\rm e}, \Lambda/R_{\rm eff}] = [100, 20]$, the chosen density contrast being relevant for flare loops (e.g., Aschwanden et al. 2004). Figure 13 presents the temporal profiles of (a) $\Gamma(t)$ and (b) $\hat{v}(R_{\rm eff}, t)$ for a variety of dimensionless loop length $L/R_{\rm eff}$ as labeled. Three features are evident regarding the periodic stage. Firstly, Figure 13b indicates that the signal for any $L/R_{\rm eff}$ further settles to a stage where $\hat{v}(R_{\rm eff}, t)$ actually possesses two periodicities. the dominant one ($P_{\rm domi}$) being close to but nonetheless longer than $\tau_{\rm long}$. In addition, the signal amplitude is modulated by a second period ($P_{\rm env} \gg P_{\rm domi}$) [8], as can be seen more clearly in Figure 13a. Secondly, when $L/R_{\rm eff}$ increases, the signal weakens and $P_{\rm domi}$ ($P_{\rm env}$) in units of $\tau_{\rm long}$ slightly decreases (increases). This feature can be seen in both Figures 13a and Figure 13b, but is clearer in the latter. Thirdly, and more importantly, the signal envelope fluctuates about a time-independent level, which can be seen by examining the profiles of the maxima/minima of either $\Gamma(t)$ or $\hat{v}(R_{\rm eff}, t)$. Given this feature, we take the relevance of evanescent modes as self-evident, and focus on the more interesting $L/R_{\rm eff}$-dependencies of $P_{\rm domi}/\tau_{\rm long}$ and $P_{\rm env}/\tau_{\rm long}$. Evidently, the envelope modulation stems from the beat among evanescent modes, which themselves possess frequencies that are marginally lower than $\omega_{\rm crit} = 2\pi/\tau_{\rm long}$. We recall that a larger $L/R_{\rm eff}$ means a larger $L/R$ and hence a smaller dimensionless axial wavenumber $kR$. We proceed to consider evanescent eigenmodes of some given radial harmonic number $l$ (say, $l = 1$ or $l = 2$ as in Figure 7 of Yu et al. 2017). Let $\omega$ denote the eigenfrequency, $P = 2\pi/\omega$ the eigen-period, and $v_{\rm ph} = \omega/k$ the phase speed. One readily finds that $P/\tau_{\rm long} = \omega_{\rm crit}/\omega = v_{\rm Ae}/v_{\rm ph}$. The reason for $P_{\rm domi}/\tau_{\rm long}$ to decrease with $L/R_{\rm eff}$ is then that the phase speeds of evanescent modes increase toward $v_{\rm Ae}$ when $kR$ decreases (see Figure 7 in Yu et al. 2017). On the other hand, that $P_{\rm env}$ increases with $L/R_{\rm eff}$ is because a reduction in $kR$ makes smaller the difference in the values of $v_{\rm ph}/v_{\rm Ae}$ for modes with adjacent values of $l$.

That evanescent modes can be seen in Figure 13 does not necessarily mean that they are observationally relevant. Consider only a fixed $\rho_{\rm i}/\rho_{\rm e} = 100$ and only the periodic stage. Let $A$ denote the maximum amplitude of $\hat{v}(R_{\rm eff}, t)$ in units of the magnitude of the initial perturbation. Experimenting with a substantial number of combinations $[L/R_{\rm eff}, \Lambda/R_{\rm eff}]$, we find that $A$ always decreases (increases) with increasing $L/R_{\rm eff}$ ($\Lambda/R_{\rm eff}$) when the other parameter is fixed, at least when

[8] Several full cycles of this periodic amplitude modulation can be seen in the time series that extends beyond, say, $120\tau_{\rm long}$. However, we choose not to show these long time series to avoid the curves becoming too crowded

$8 \leq L/R_{\rm eff} \leq 15$ and $0 < \Lambda/R_{\rm eff} \leq 20$. Suppose that evanescent modes can be seen as observationally relevant only when $A$ exceeds some threshold $A_{\rm c}$, and let $(L/R_{\rm eff})_{\rm c}$ denote the critical $L/R_{\rm eff}$ beyond which $A < A_{\rm c}$. Seeing $A_{\rm c}$ as variable, this then means that $(L/R_{\rm eff})_{\rm c}$ is a function of $A_{\rm c}$. Figure 14 displays the $A_{\rm c}$-dependence of $(L/R_{\rm eff})_{\rm c}$ for a number of $\Lambda/R_{\rm eff}$ as labeled, before describing which we need to mention some technical subtlety. We consistently adopt the timeframe $t \leq 40\tau_{\rm long}$ to determine $A$ and eventually construct a symbol in Figure 14. However, Figure 13a has already shown that $P_{\rm env}$ becomes longer when $L/R_{\rm eff}$ increases, making it possible that the amplitude maximum is not captured for $t \leq 40\tau_{\rm long}$ if $P_{\rm env}$ is too long. This turns out not to be a real concern for two reasons, one being that one needs to specify a timeframe in any case, and the other being that the envelope modulation is already clear for $t \leq 40\tau_{\rm long}$. We will return to this point later. Now let "allowed range" refer specifically to those $L/R_{\rm eff}$ for which evanescent modes are visible. One sees from Figure 14 that $(L/R_{\rm eff})_{\rm c}$ decreases monotonically with $A_{\rm c}$ for a given $\Lambda/R_{\rm eff}$, meaning that the "allowed range" narrows when the relevant instrumental sensitivity weakens. Likewise, $(L/R_{\rm eff})_{\rm c}$ increases when $\Lambda/R_{\rm eff}$ increases, meaning that the "allowed range" broadens with increasing $\Lambda/R_{\rm eff}$ for a given sensitivity and hence a given $A_{\rm c}$.

It should be informative to place Figure 14 in the ER83 context. Consider an "ER" loop, by which we mean a loop with an equilibrium density $\rho_0(r)$ that equals $\rho_{\rm i}$ for $r < R_{\rm eff}$ but $\rho_{\rm e}$ otherwise. Restrict ourselves to axial fundamentals. A critical $(L/R_{\rm eff})_{\rm ER}$ then follows from Equation (A1),

$$(L/R_{\rm eff})_{\rm ER} = \frac{\pi\sqrt{\rho_{\rm i}/\rho_{\rm e} - 1}}{j_{0,1}}, \tag{C23}$$

only below which evanescent modes are possible in an ER loop. With Equation (C23) one finds that $(L/R_{\rm eff})_{\rm ER}$ evaluates to 13 for $\rho_{\rm i}/\rho_{\rm e} = 100$, and this value is represented by the horizontal dash-dotted line in Figure 14. Two situations arise regarding the relevance of $(L/R_{\rm eff})_{\rm ER}$, to describe which we assume that $L/R_{\rm eff}$ is known observationally and that a time series is available for the pertinent observable over tens of longitudinal Alfvén times. First consider the situation where $L/R_{\rm eff}$ is observed to exceed $(L/R_{\rm eff})_{\rm ER}$. Suppose that the observed signal eventually possesses a stage where the amplitude does not diminish with time. It then follows from the left corner of Figure 14 that this stage cannot be interpreted in the ER83 framework, because no evanescent modes can be excited regardless of $\Lambda$. In this regard, a diffuse loop model such as formulated by the outer-$\mu$ profile may indeed broaden the range of flare-associated QPPs that FSMs may account for. However, this broadending is rather limited because it happens only when the relevant instrument is highly sensitive and $\Lambda/R_{\rm eff}$ is nearly beyond the range that we deem observationally realistic. Now consider the situation where $L/R_{\rm eff}$ is observed to be smaller than $(L/R_{\rm eff})_{\rm ER}$. Evanescent modes are allowed by ER loops in this case, and are visible for the majority of combinations $[A_{\rm c}, \Lambda/R_{\rm eff}]$ explored in Figure 14 for our outer-$\mu$ loops. One may then question whether the temporal profile of the pertinent observable can help categorize the involved flare loop as an ER loop or an outer-$\mu$ one. This is indeed possible, to illustrate which we consider the case where $L/R_{\rm eff} = 11$. Suppose that the flare loop is describable as an ER loop. Equation (C23) then yields a value of 5.66 if one replaces $j_{0,1} = 2.41$ therein with $j_{0,2} = 5.52$. This means that the evanescent mode with radial harmonic number $l = 2$ is not relevant, and the pertinent signal eventually settles to a monochromatic variation with a constant amplitude. Now suppose that the flare loop agrees with an outer-$\mu$ loop for which $\mu$ is presumed to be 1.5, and suppose further that $\Lambda/R_{\rm eff} = 10$. It turns out that the $\hat{v}(R_{\rm eff}, t)$ profile is very similar

to the black curve in Figure 13b, even though the amplitude maximum $A$ in the periodic stage attains a smaller value of $\sim 0.1$. Nonetheless, it an amplitude of this magnitude can be resolved, then the relevant observable will be seen to experience some envelope modulation, which is distinct from what is expected for an ER loop. In addition, this amplitude modulation may also be useful to distinguish between kink modes and FSMs in flare loops, if flare loops are not well spatially resolved to tell whether they are experiencing transverse displacements. We refrain from discussing this aspect further for two reasons, one being that kink modes in our outer-$\mu$ setup have yet to be examined, and the other being that a dedicated forward modeling approach seems necessary to establish the detailed observational signatures. Rather, with Figure 14 we conclude that whether evanescent modes in outer-$\mu$ loops can be observed depends critically on instrumental sensitivity. We conclude further that the ER83 cutoff $(L/R_{\rm eff})_{\rm ER}$ serves as a useful reference in that evanescent modes in outer-$\mu$ loops are hardly observable when $L/R_{\rm eff} \geq (L/R_{\rm eff})_{\rm ER}$ unless the pertinent instrument is extremely sensitive.

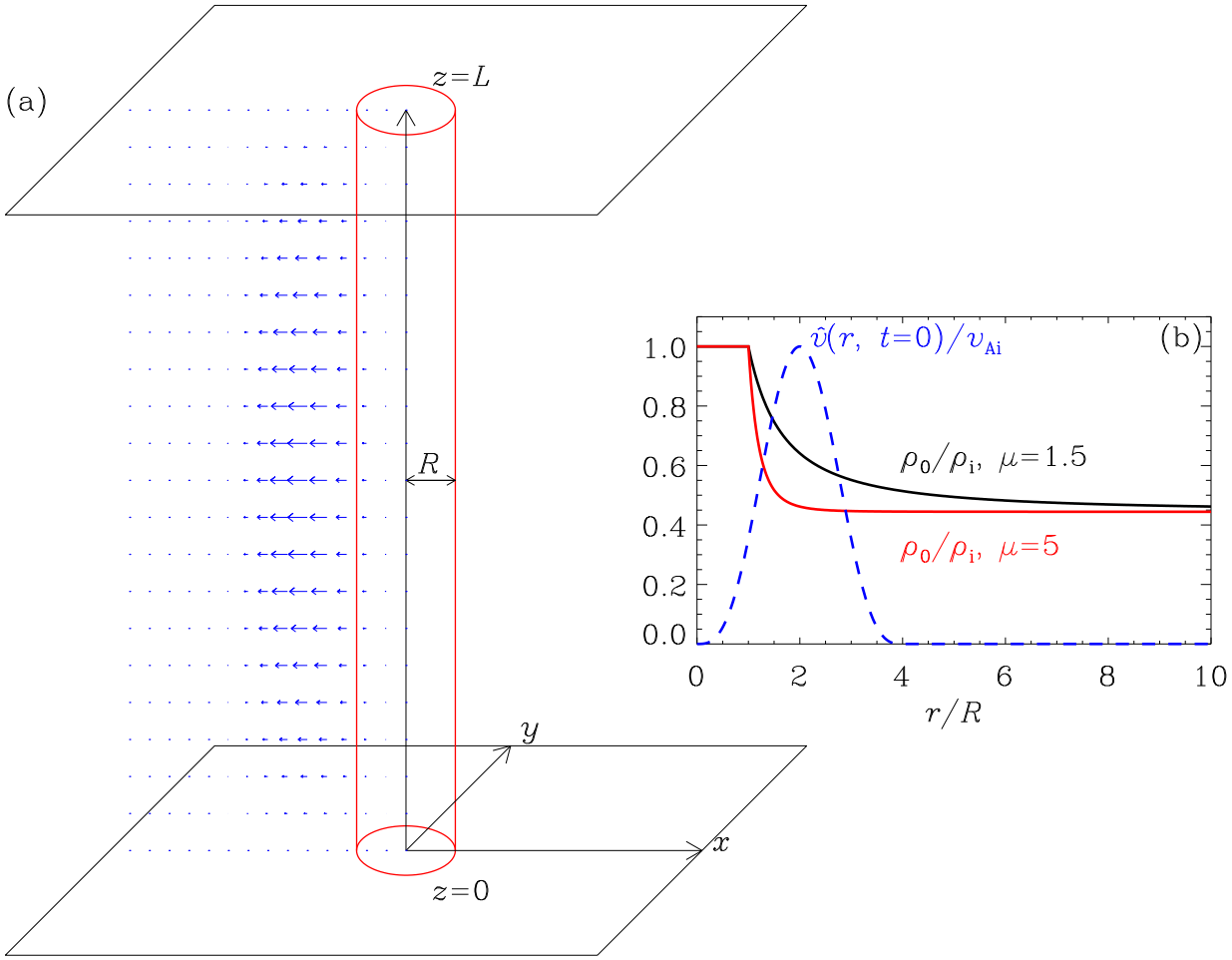


**Figure 1.** (a) Illustration of the equilibrium configuration, together with the initial velocity field in an arbitrary plane through the cylinder axis (the blue arrows). The $z$-dependence of the initial perturbation leads to axial fundamentals. (b) Radial profiles of the initial perturbation ($\hat{v}$, the blue dashed curve) and the equilibrium density ($\rho_0$, the solid curves), both involved in IVP 1. The density contrast $\rho_i/\rho_e$ is chosen to be 2.25. Two steepness parameters are examined, namely $\mu = 1.5$ (the black curve) and $\mu = 5$ (red).

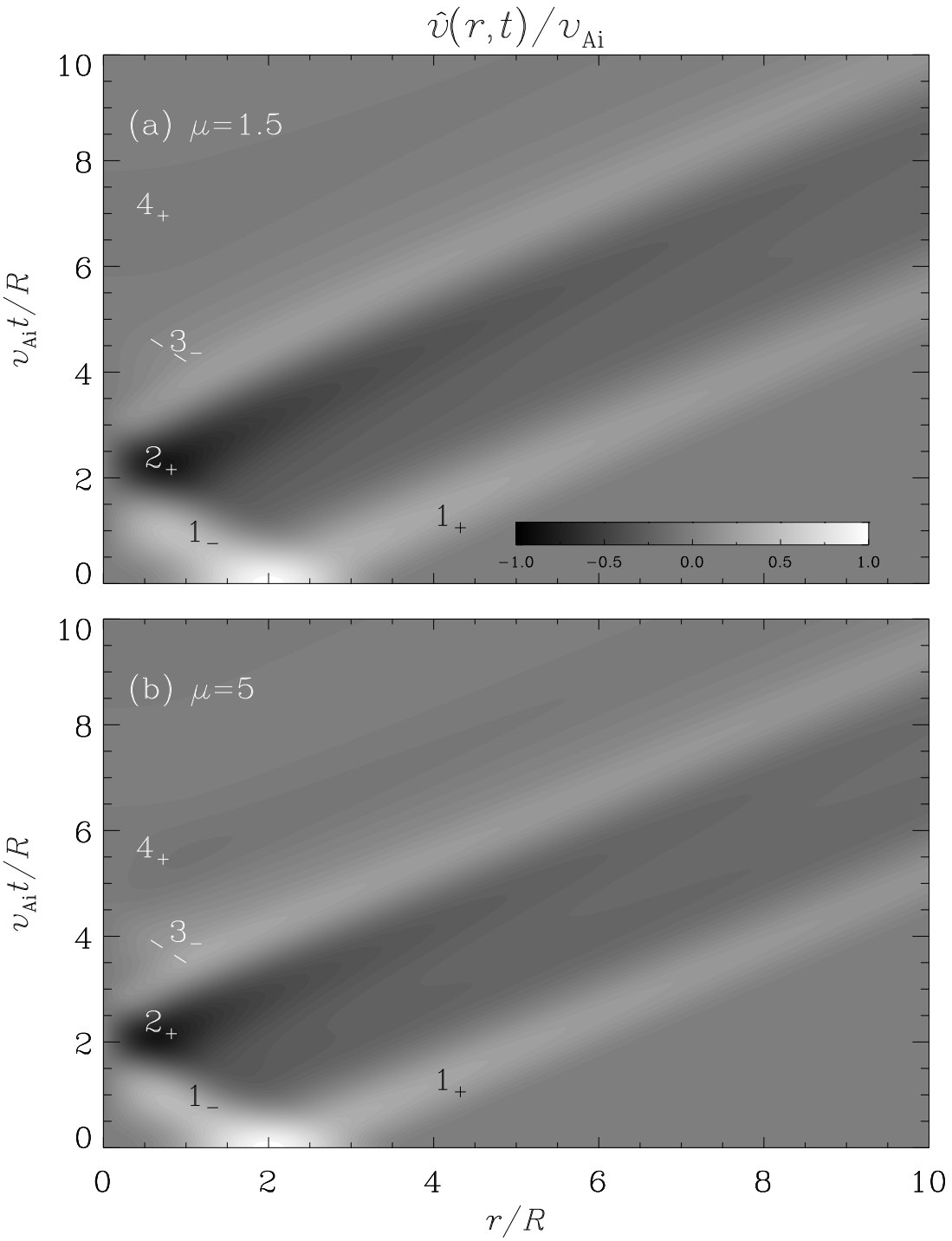


**Figure 2.** Finite-difference (FD) solutions to IVP 1 for equilibrium density profiles with the steepness parameter being (a) $\mu = 1.5$ and (b) $\mu = 5$. Plotted are the distributions of the radial speed $\hat{v}$ in the $r - t$ plane. Some prominent wavefronts are singled out as labeled, with the plus (minus) sign representing outward (inward) propagation. Both computations pertain to the combination $[\rho_{\rm i}/\rho_{\rm e}, kR, \Lambda/R] = [2.25, \pi/15, 4]$.

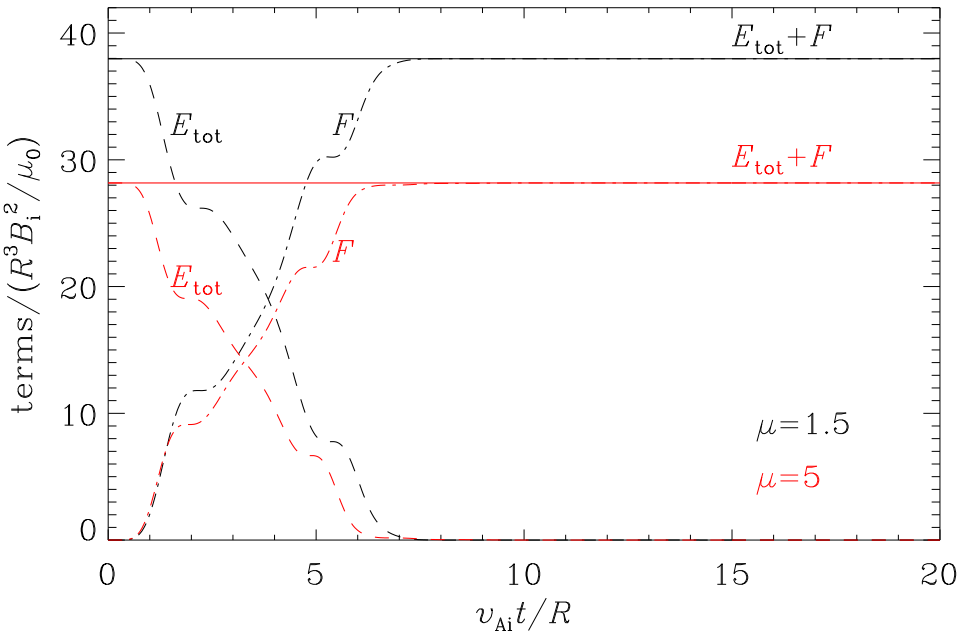


**Figure 3.** Temporal variations of some terms characterizing the energetics of axisymmetric perturbations in the cylindrical volume ($V$) where the initial perturbation is applied. The dashed curves labeled $E_{\rm tot}$ represent the total wave energy in $V$, while the dash-dotted curves represent the cumulative energy loss from $V$ and are labeled $F$ (see Equations (12) and (13) for definitions). Their sum is plotted by the solid curves. The energetics terms are evaluated with the finite-difference solutions to IVP 1 for two steepness parameters, one being $\mu = 1.5$ (the black curves) and the other being $\mu = 5$ (red). Both computations pertain to the combination $[\rho_{\rm i}/\rho_{\rm e}, kR, \Lambda/R] = [2.25, \pi/15, 4]$.

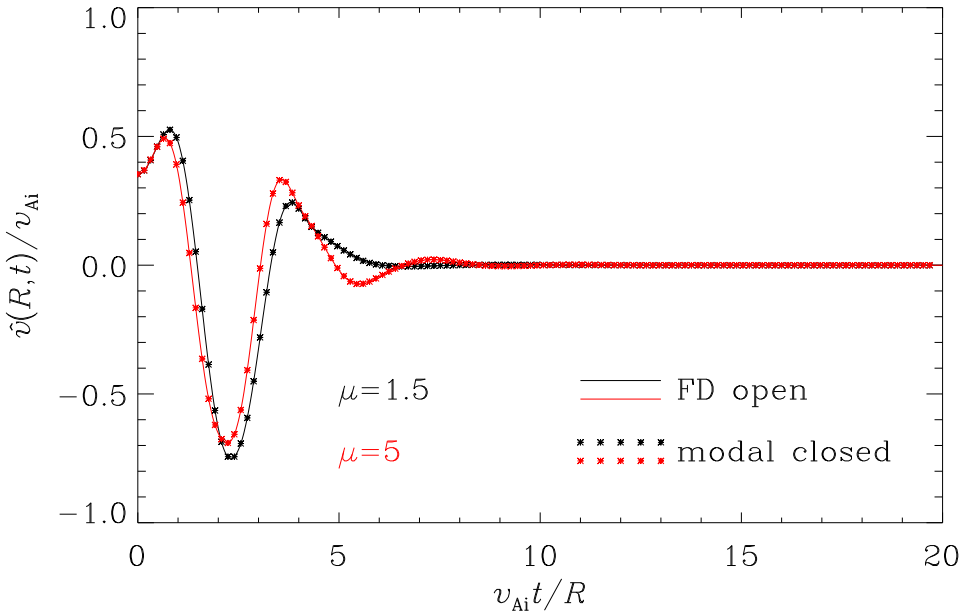


**Figure 4.** Temporal evolution of the radial speed at $r = R$ as found by solving IVP 1 for two steepness parameters, one being $\mu = 1.5$ (the black curves and symbols) and the other being $\mu = 5$ (red). All computations pertain to the combination $[\rho_{\rm i}/\rho_{\rm e}, kR, \Lambda/R] = [2.25, \pi/15, 4]$. Two independent methods are adopted to solve IVP 1. The finite-difference solutions are represented by the solid curves, labeled "FD open" because this approach directly applies to a radially open system. The modal solutions are given by the asterisks, labeled "modal closed" because the solutions are based on eigenmodes on a closed domain (see Equation (23)). A domain of size $d = 50\ R$ is employed here.

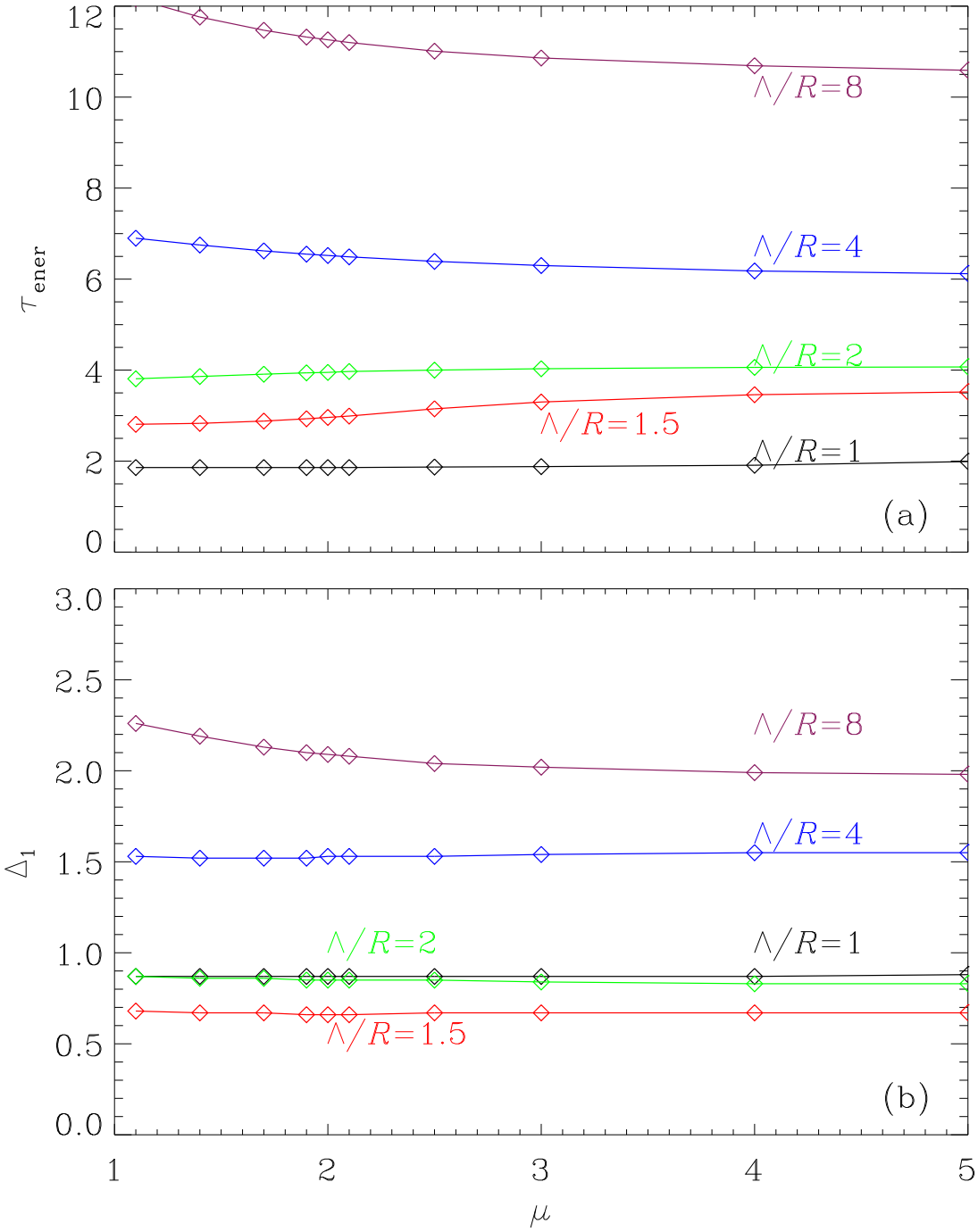


**Figure 5.** Dependencies of (a) $\tau_{\rm ener}$ and (b) $\Delta_1$ on the steepness parameter $\mu$ for a number of values of the spatial extent of the initial perturbation ($\Lambda$) as labeled. Here $\tau_{\rm ener}$ denotes the time at which the total wave energy in the cylindrical volume laterally bounded by $r = \Lambda$ drops from its initial value by a factor of $e^4 \approx 55$. Furthermore, $\Delta_1$ denotes the temporal spacing between the first two extrema in the $\hat{v}(R,t)$ profile. All results are found by solving IVP 1 with the finite-difference approach, and the combination $[\rho_{\rm i}/\rho_{\rm e}, kR]$ is fixed at $[2.25, \pi/15]$.

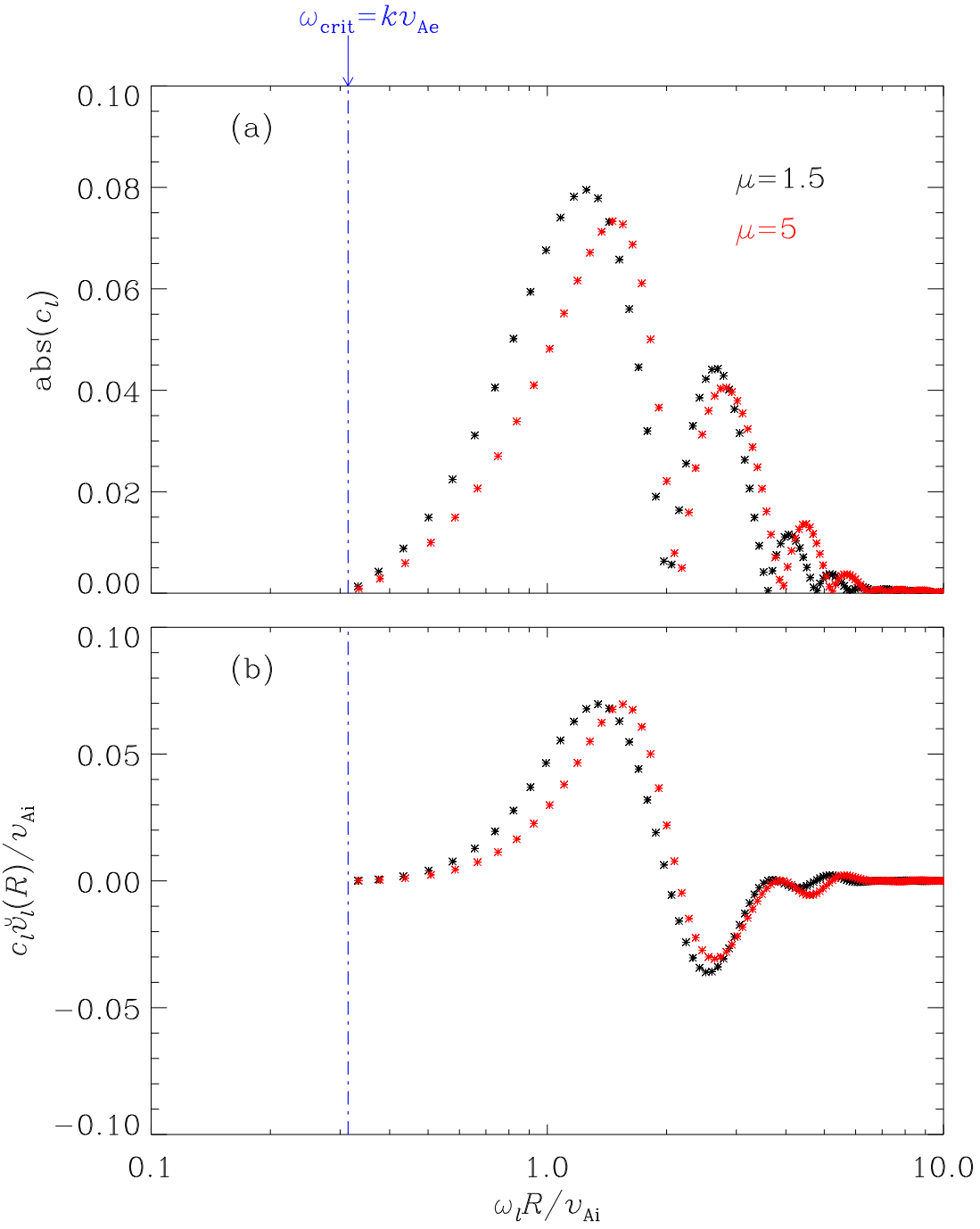


**Figure 6.** Frequency-dependencies of the contributions of individual modes to the modal solutions for a fixed combination $[\rho_{\rm i}/\rho_{\rm e}, kR, \Lambda/R, d/R] = [2.25, \pi/15, 4, 50]$. Two steepness parameters are examined, one being $\mu = 1.5$ (the black asterisks) and the other being $\mu = 5$ (red). Plotted are (a) the modulus of the position-independent coefficient $c_l$, and (b) the specific contribution $c_l\breve{v}_l(r)$ evaluated at $r = R$. The critical frequency $\omega_{\rm crit} = kv_{\rm Ae}$ is marked by the vertical dash-dotted lines for reference.

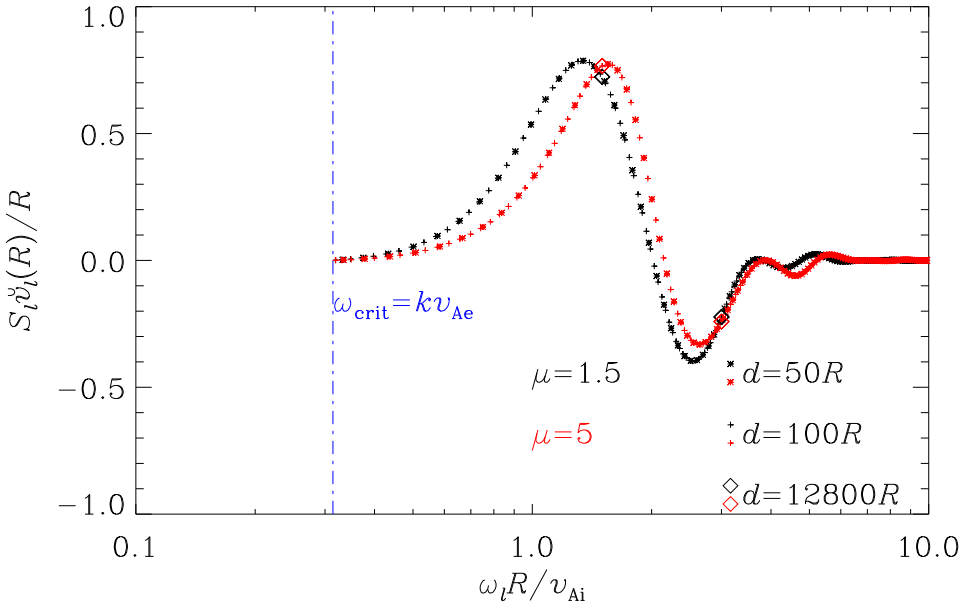


**Figure 7.** Frequency-dependencies of the spectral density $S_l\check{v}_l(r)$ evaluated at $r = R$ involved in the modal solutions for a fixed combination $[\rho_{\rm i}/\rho_{\rm e}, kR, \Lambda/R] = [2.25, \pi/15, 4]$. Two steepness parameters are examined, one being $\mu = 1.5$ (the black symbols) and the other being $\mu = 5$ (red). The modal solutions are based on eigenmodes on a closed domain, for which three different sizes ($d$) are experimented with. Note that only two small subsets of modes are presented for the domain with $d/R = 12800$. See text for details.

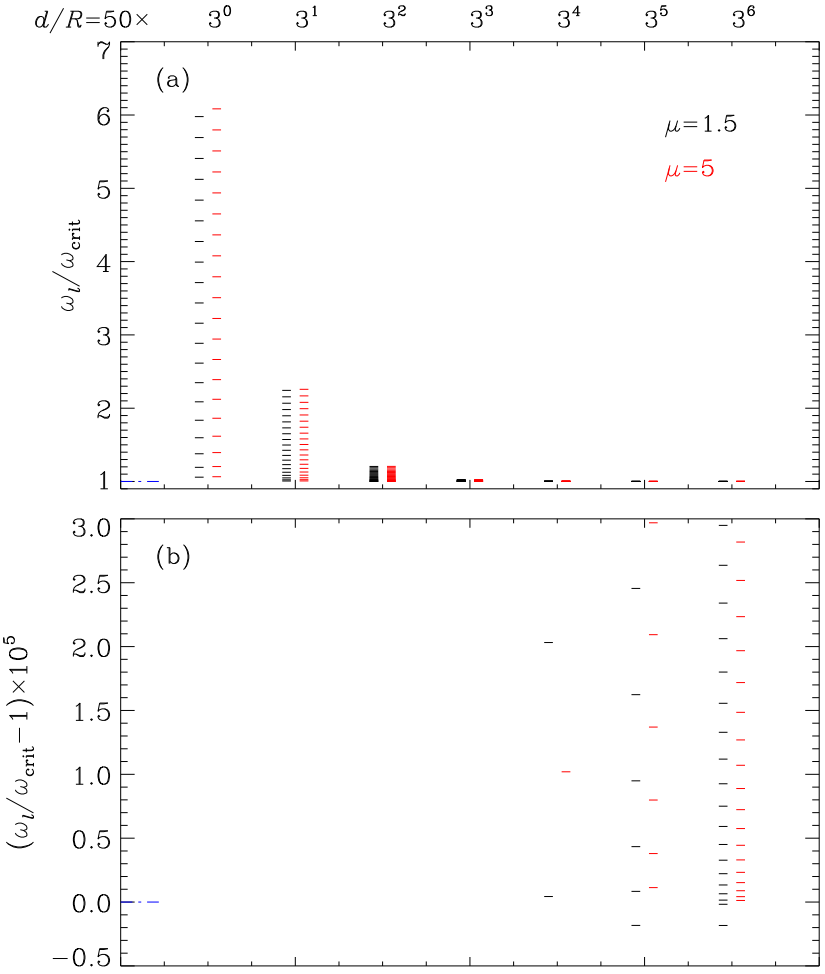


**Figure 8.** Eigenfrequency diagrams ("level schemes") for the first 20 modes found by solving EVP 1 for a fixed combination $[\rho_{\rm i}/\rho_{\rm e}, kR] = [2.25, \pi/15]$. Two steepness parameters are examined, one being $\mu = 1.5$ (the black ticks) and the other being $\mu = 5$ (red). A number of domain sizes ($d$) are examined as labeled, and the mode frequencies with a given $\mu$ are represented by the horizontal ticks stacked vertically for a given $d$. Plotted are (a) the mode frequencies in units of $\omega_{\rm crit} = kv_{\rm Ae}$, and (b) the fractional difference of mode frequencies from $\omega_{\rm crit}$. Note that this fractional difference is multiplied by a factor of $10^5$.

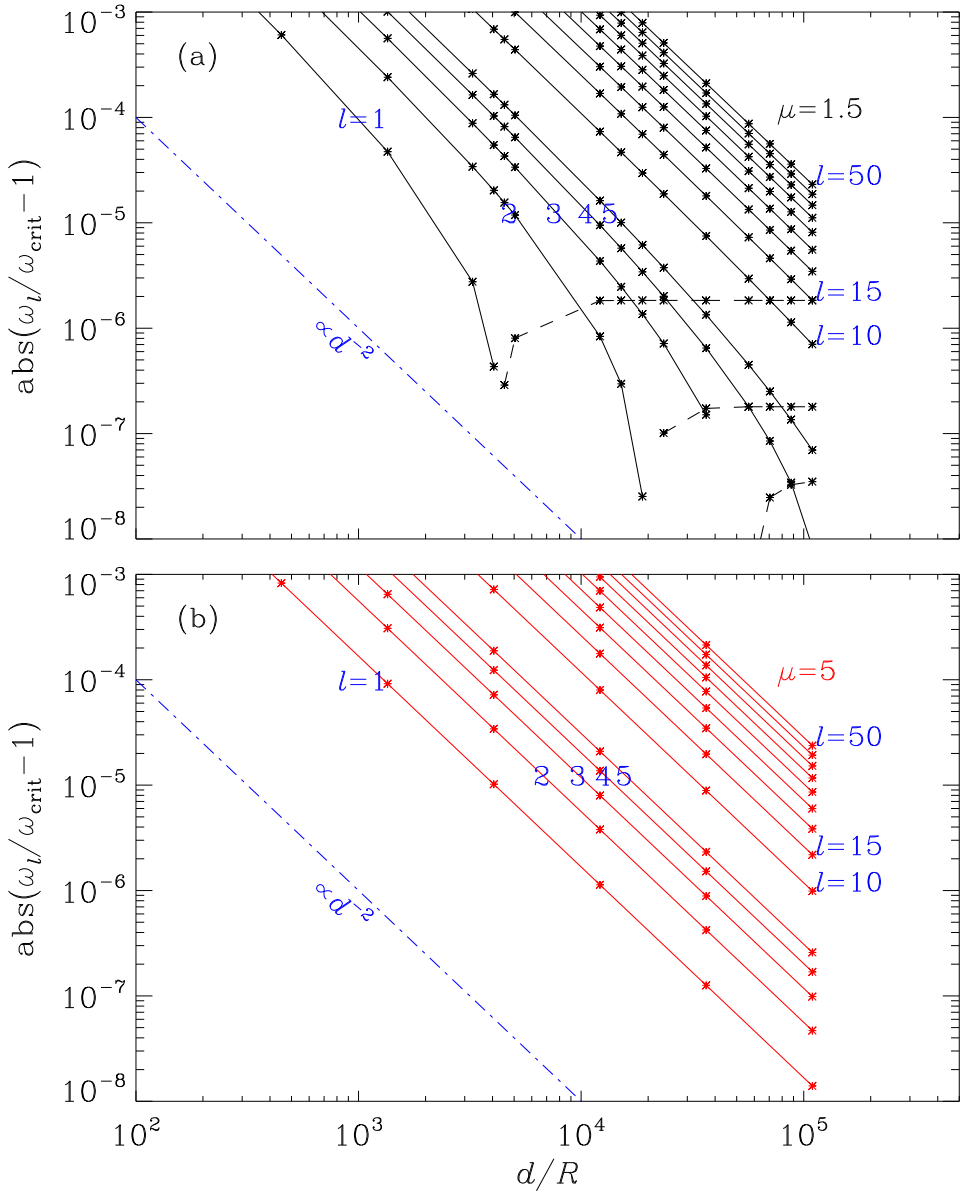


**Figure 9.** Dependencies on the dimensionless domain size ($d/R$) of the modulus of the fractional difference $\delta_l = \omega_l/\omega_{\rm crit} - 1$ as found by solving EVP 1 for a steepness parameter being (a) $\mu = 1.5$ and (b) $\mu = 5$. The combination $[\rho_{\rm i}/\rho_{\rm e}, kR]$ is fixed at $[2.25, \pi/15]$. For each pair $[\mu, d/R]$, the first five modes are always presented, while the rest are evenly sampled with a step of five in $l$ when $l$ ranges from 10 to 50. In addition, $|\delta_l|$ for a given $l$ is connected by a solid (dashed) curve when $\delta_l$ is positive (negative). The blue dash-dotted line represents a $1/d^2$-dependence for comparison. See text for details.

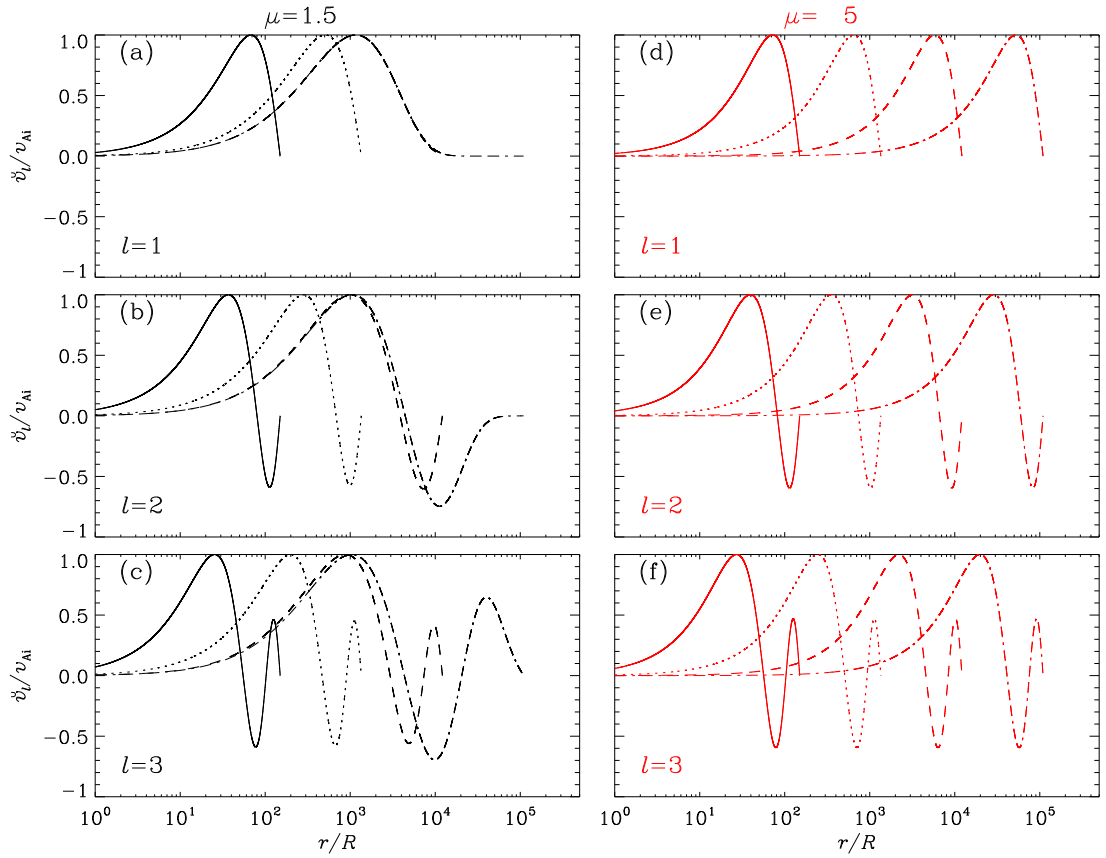


**Figure 10.** Radial profiles of the first three eigenfunctions as found by solving EVP 1 on a variety of domains differentiated by the linestyles. The combination $[\rho_i/\rho_e, kR]$ is fixed at $[2.25, \pi/15]$. Two steepness parameters are examined, one being $\mu = 1.5$ (the left column) and the other being $\mu = 5$ (right). The eigenfunctions are arbitrarily rescaled to better visualize the differences between different domain sizes.

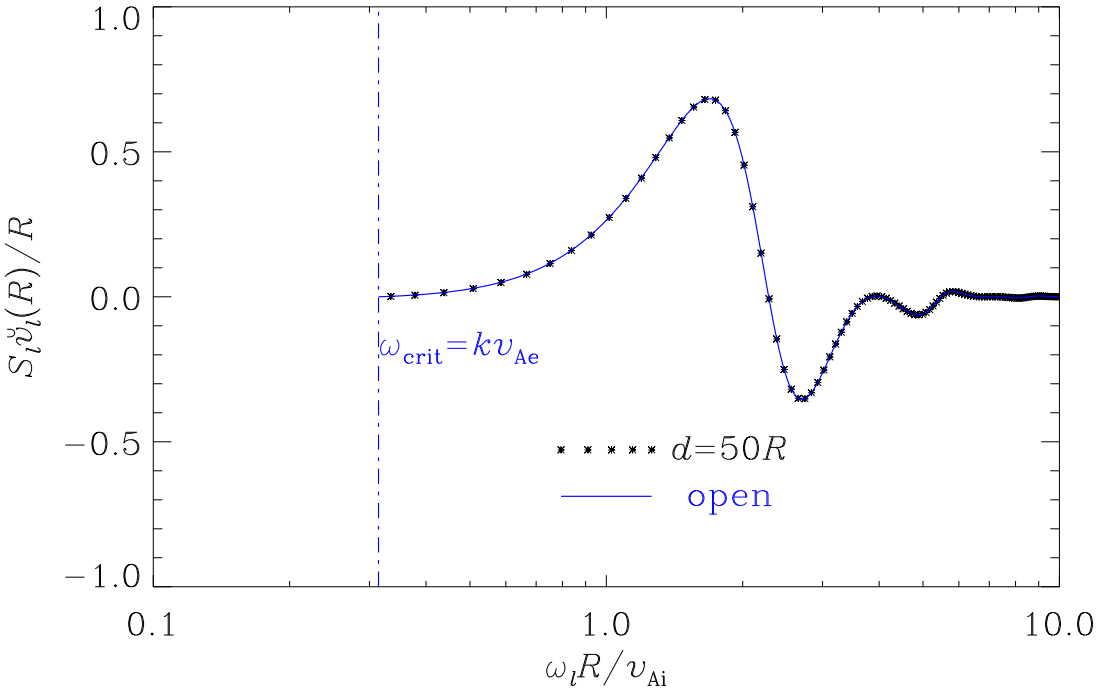


**Figure 11.** Frequency-dependencies of spectral densities $S\breve{v}(r)$ evaluated at $r = R$ as found by solving IVP 1 for a coronal cylinder with a step density profile. The combination $[\rho_{\rm i}/\rho_{\rm e}, kR, \Lambda/R]$ is fixed at $[2.25, \pi/15, 4]$. The asterisks represent the discrete modes pertinent to EVP 1 on a domain with $d/R = 50$, whereas the blue solid curve represents the continuum of improper eigenmodes on a radially open system. The vertical dash-dotted line marks the critical frequency $\omega_{\rm crit} = kv_{\rm Ae}$. See text for details.

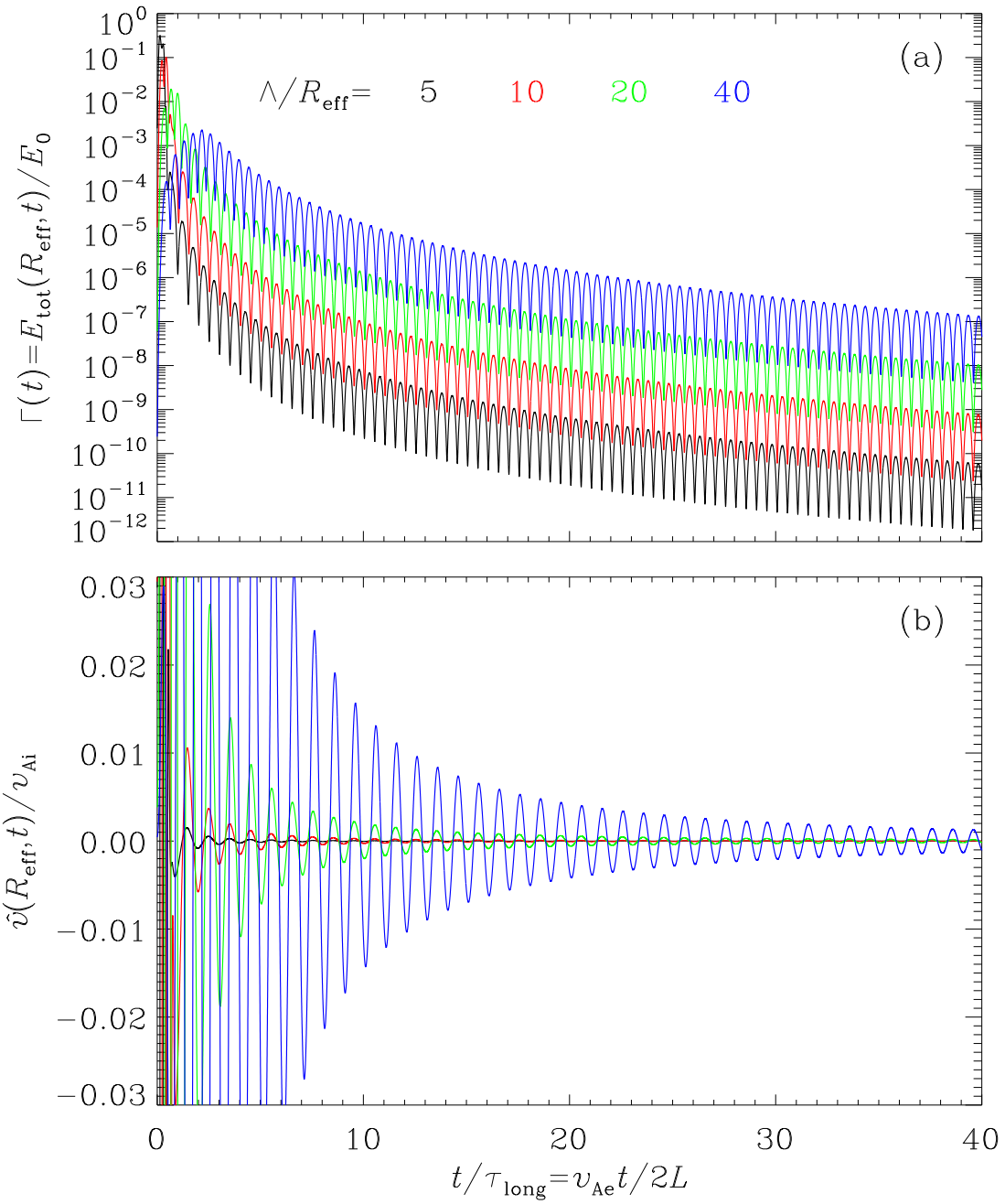


**Figure 12.** Temporal profiles for (a) the energy fraction $\Gamma(t)$ and (b) the radial speed $\hat{v}(R_{\rm eff},t)$ for a loop with $[\rho_{\rm i}/\rho_{\rm e}, L/R_{\rm eff}] = [10, 10]$. The steepness parameter is fixed at $\mu = 1.5$, while a number of values are examined for the spatial extent of the initial perturbation as labeled. All solutions are found with the finite-difference approach. Here $R_{\rm eff}$ represents the effective loop radius, and $\Gamma(t)$ measures the total energy in the volume $r \leq R_{\rm eff}$ in units of the energy imparted to the entire system by the initial perturbation. Note that $\hat{v}(R_{\rm eff},t)$ is measured in units of the magnitude of the initial velocity perturbation. See text for details.

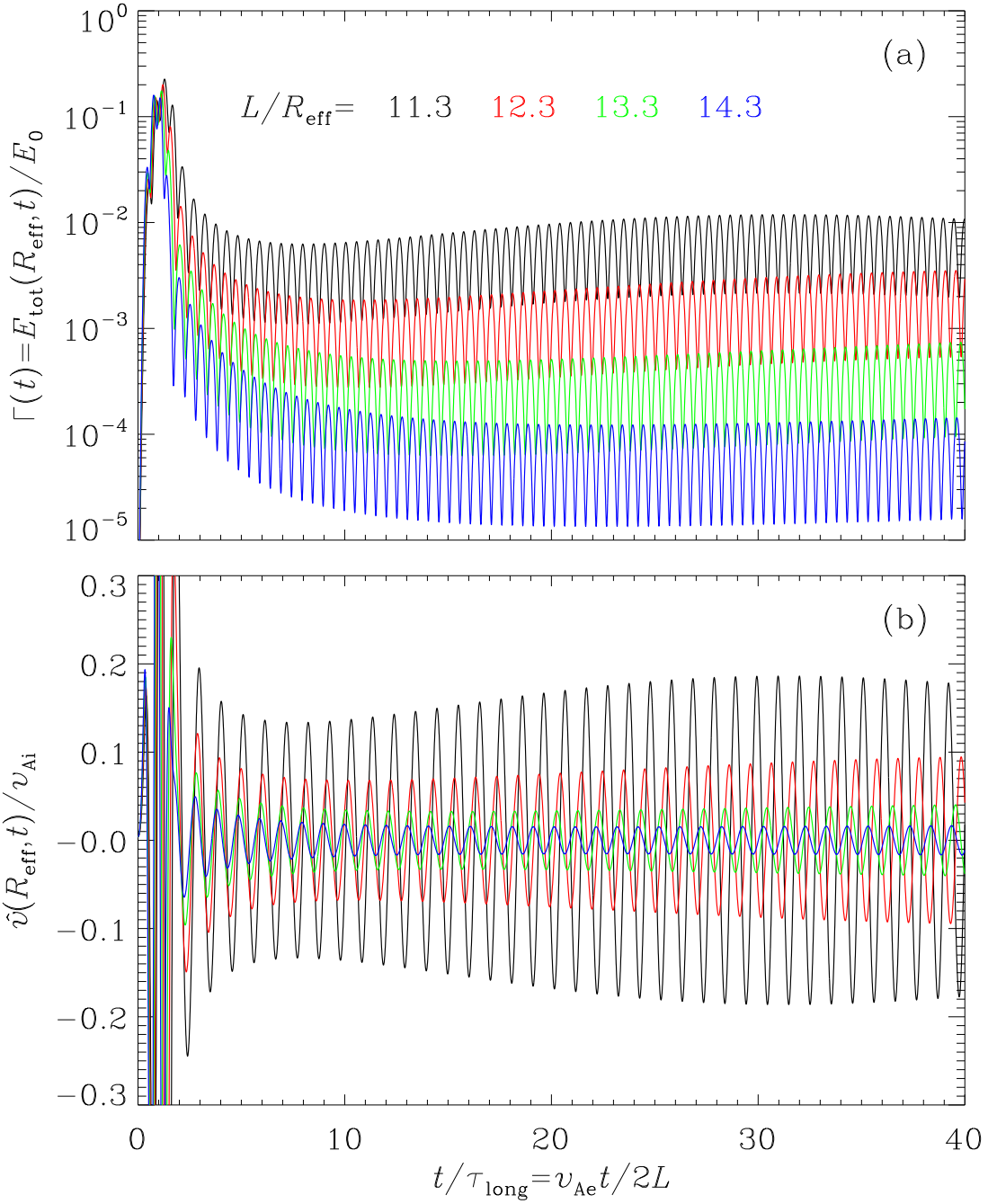


**Figure 13.** Similar to Figure 12 but for $[\rho_{\rm i}/\rho_{\rm e}, \Lambda/R_{\rm eff}] = [100, 20]$. The steepness parameter is fixed at $\mu = 1.5$, while a number of values are examined for $L/R_{\rm eff}$ as labeled. See text for details.

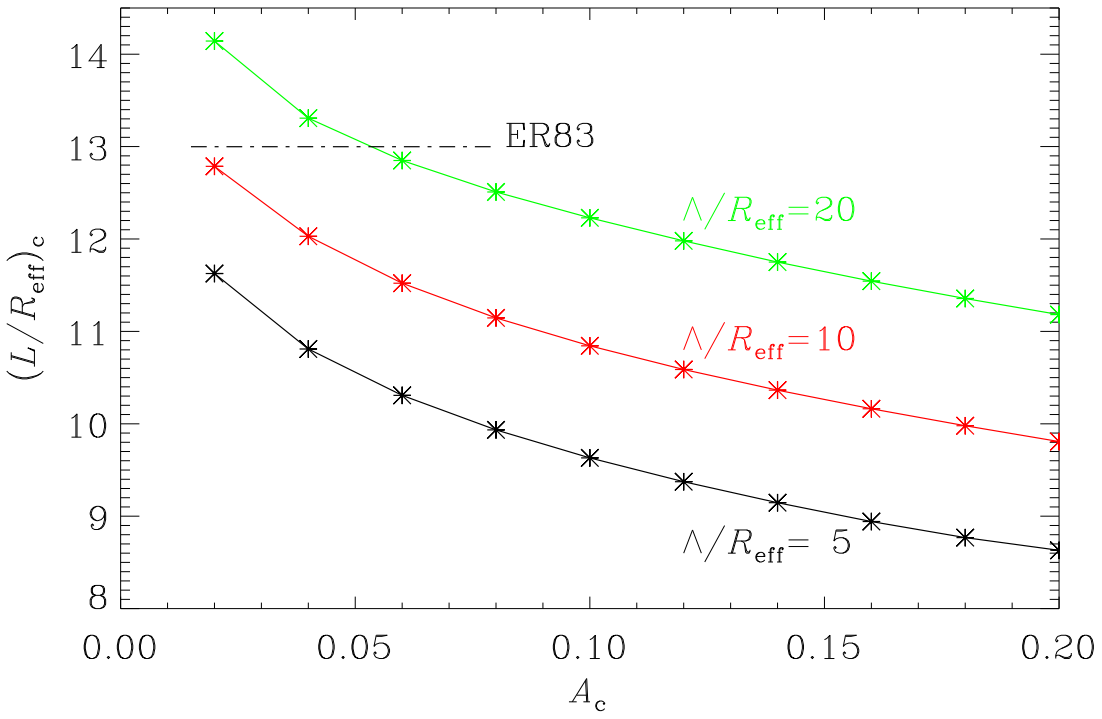


**Figure 14.** Dependence of the critical $(L/R_{\rm eff})_{\rm c}$ on the critical dimensionless amplitude $A_{\rm c}$ for a number of $\Lambda/R_{\rm eff}$ as labeled. The combination $[\rho_{\rm i}/\rho_{\rm e}, \mu]$ is fixed at $[100, 1.5]$. For a given $\Lambda/R_{\rm eff}$, a loop with $L/R_{\rm eff}$ larger (smaller) than $(L/R_{\rm eff})_{\rm c}$ yields a $\hat{v}(R_{\rm eff}, t)$ for which the maximum amplitude in the periodic stage is smaller (larger) than $A_{\rm c}$ when measured in units of the magnitude of the initial velocity perturbation. The horizontal dash-dotted line represents the expectation within the ER83 framework ($(L/R_{\rm eff})_{\rm ER}$) for a piece-wise uniform loop where the equilibrium density attains $\rho_{\rm i}$ for $r \leq R_{\rm eff}$ but $\rho_{\rm e}$ otherwise. Evanescent modes are not relevant when $L/R_{\rm eff} < (L/R_{\rm eff})_{\rm ER}$ in this framework. See text for details.